UNIVERSITEIT ANTWERPEN

Improved low energy optics control at the CERN Proton Synchotron

Auteur:
Wietse VAN GOETHEM

Supervisor:
Dr. Alexander HUSCHAUER

Prof. Dr. Pierre VAN MECHELEN

Proefschrift ter verkrijging van de graad van Master in de Fysica

Departement Fysica
Faculteit Wetenschappen
Universiteit Antwerpen

January 4, 2021

Abstract

English abstract

The CERN Proton Synchrotron (PS) is a versatile and reliable accelerator that has produced a multitude of beams for fixed target experiments and higher-energy accelerators such as the Large Hadron Collider (LHC). During the current Long Shutdown 2 (LS2) the PS is being upgraded in the framework of the LHC Injectors Upgrade (LIU) project with the aim of producing LHC-type beams of even higher-brightness. In this thesis the research performed to investigate and mitigate emittance blow-up observed at injection energy of high-brightness beams is presented. The investigation of beam blow-up is essential to reach the desired properties for LIU beams. The first part of the thesis focuses on optimising the lattice optics to reduce β- and dispersion-beating by re-positioning the Low Energy Quadrupoles (LEQs). The optics beatings are quantified and quadrupole configurations are obtained that can reduce the emittance blow-up by ≈ 35 % at the working point (6.10, 6.24) in the horizontal plane or by ≈ 65 % at the working point (6.21, 6.10) in the vertical plane. One of the new quadrupole configurations is easily testable as it requires to only remove a single quadrupole from the current lattice. For the second part, the dispersive contributions are deconvoluted from horizontal beam profile measurements through achieving zero-dispersion optics at the measurement location using the LEQs. The number of LEQs and the LEQ strengths are optimised for each beam measurement location to reduce optics beating through numerical optimisation. The dispersion moves faster to zero with the inclusion of space charge effects, thus the experimental optics beatings will be less than the simulated ones. The final investigation presented in this thesis looks at the accuracy of measuring the betatronic contributions of the beam emittance. The β-function is measured through K-modulation at an LEQ during a magnetic plateau of a measurement cycle. The characteristics of the modulation and the number of required cycles to achieve an accuracy of 1% on the reconstructed β-function were studied. Additionally, the impact of a transfer factor error on the final β-function was investigated.

Nederlandstalig abstract

De CERN Proton Synchrotron (PS) is een veelzijdige en betrouwbare versneller die een veelvoud aan deeltjesbundels heeft geproduceerd voor vaste-doel experimenten en voor hoge-energieversnellers zoals de Large Hadron Collider (LHC). Tijdens de huidige Long Shutdown 2 (LS2) wordt de PS bijgewerkt als onderdeel van de high-Luminosity Injector Upgrade (LIU) van de LHC om bundels van hogere intensiteit te bereiken. In dit proefschrift wordt de sterke groei van de emissiecoëfficient van hoge-intensiteitsbundels tijdens de injectiefase onderzocht, evenals hoe deze kan worden verminderd. Dit onderzoek is essentieel om de gewenste doelstellingen voor de LIU te bereiken. Het eerste deel van het proefschrift richt zich op de optimalisatie van de bundeloptiek om de β en dispersie fluctuaties te verminderen door de lage-energie quadrupolen (LEQs) te herpositioneren. De bundeloptiek wordt gekwantificeerd en quadrupoolconfiguraties worden verkregen die de groei van de emissiecoëfficient kan verminderen met $\approx$ 35 % op het werkpunt (6.10, 6.24) in het horizontale vlak of met $\approx$ 65 % op het werkpunt (6.21, 6.10) in het verticale vlak. Eén van de nieuwe quadrupoolconfiguraties is eenvoudig te testen, omdat er maar één quadrupool van het huidige raster hoeft te worden verwijderd. In het tweede deel van de thesis worden de dispersieve bijdragen gedeconvolueerd van horizontale bundelprofielmetingen, door een nul-dispersie optiek op de meetlocatie op te leggen met behulp van de LEQs. Het aantal LEQs en hun sterktes zijn numeriek geoptimaliseerd op elke meetlocatie om de distorsie van de optiek tegen te gaan. De dispersie gaat sneller naar nul door het includeren van spacecharge-effecten, waardoor de experimentele distorsie van de bundeloptiek minder groot zal zijn dan de gesimuleerde. In het laatste deel van het proefschrift wordt gekeken naar de precisie van de betatronische bijdragen aan de emissiecoëfficient-metingen. De β-functie wordt gemeten door middel van de zogenaamde K-modulatie op een LEQ tijdens het eerste magnetische plateau van een magnetische cyclus. De karakteristieken van de modulatie en het aantal cycli worden bestudeerd om een precisie van 1 % te hebben op de gereconstrueerde β-functie. Ten slotte, werd de impact van een fout in de overdrachtsfactor op de uiteindelijke β-function onderzocht.

Acknowledgements

During the exceptional experience that was the year 2020, I was given the amazing opportunity to work as a technical student at CERN. Today, I am able to give my thanks to those who gave me this possibility, and to those who have aided and inspired me along this journey.
First and foremost, I would like to give my deepest thanks to my CERN supervisor, Alexander Huschauer. Working with you was an enormous pleasure. Your never-ending guidance, support and knowledge made this year incredible and allowed me to learn so much from you.
Furthermore, I will be forever indebted to Massimo Giovanozzi and Frederik Van der Veken, for making this studentship a possibility, providing me with a multitude of enlightening discussions, proofreading my thesis, and the countless other things you have done for me. Thank you.
I would like to express my gratitude to Haroon Rafique for the explanations concerning the space charge framework and answering my numerous questions, no matter how trivial they might have been.
I would like to acknowledge all of the BE staff and my fellow CERN students for their hospitality and helpfulness. I am looking forward to our continued work in the future.
Ik wil ook graag danku zeggen aan mijn vrienden en familie, vooral mijn gezin, die me hebben gesteund doorheen heel mijnn studie en voor de vele onvergetelijke momenten dat we hebben kunnen delen.
Ik kan niet anders dan mijn DnD groepje erkennen want jullie vriendschap betekent de wereld voor mij en een intro schrijven zonder dat jullie hem onderbreken zou heel onnatuurlijk aanvoelen.

Tenslotte, wil ik Elena bedanken voor al de liefde, bemoediging en plezier die je toebrengt aan mijn leven. Ik kijk er naar uit om deze reis samen met jou verder te zetten.

Contents

List of Acronyms

BBQ	**B**ase **B**and **T**une measurement system
BGI	**B**eam **G**as **I**onization monitor
CERN	**E**uropean **O**rganisation for **N**uclear **R**esearch
CVXOPT	public library **P**ython **S**oftware for **C**onvex **O**ptimization
LEP	**L**arge **E**lectron-**P**ositron collider
LEQ	**L**ow **E**nergy **Q**uadrupole
LHC	**L**arge **H**adron **C**ollider
LIU	LHC **I**njectors **U**pgrade
MAD	**M**ethodical **A**ccelerator **D**esign
MU	**M**agnet **U**nit
PFW	**P**ole **F**ace **W**inding
PS	**P**roton **S**ynchotron
PSB	**P**roton **S**ynchotron **B**ooster
RF	**R**adio **F**requency
SEM	**S**econdary **E**lectron **EM**ission
SPS	**S**uper **P**roton **S**ynchotron
SS	**S**traight **S**ection
WS	**W**ire **S**canner

1 Introduction

The European Organization for Nuclear Research (CERN) has been at the forefront of energy-frontier particle physics research since its foundation in 1954. Currently, a large part of fundamental particle physics research is, in layman's terms, done by accelerating charged particles, colliding them and detecting the end products. To reach higher and higher energies, particle accelerators, detectors, and other infrastructure have become extremely complex. The Proton Synchrotron (PS) is one of these accelerators and it was CERN's flagship accelerator until new accelerators were build in the 1970s. Currently, the PS supplies particle beams to higher-energy accelerators and to the downstream fixed-target facilities.

The research presented in this thesis is focused on improving the control of the PS optics functions at injection energies. Currently, large transverse emittance blow-up is generated at working points close to the integer resonances when the tunes are controlled by means of the Low Energy Quadrupoles (LEQs). The emittance blow-up is a consequence of the beatings of the optics functions caused by the irregular distribution of the LEQs around the ring, which leads to resonance excitation, and the large direct space charge tune spread of the operational beams produced for the Large Hadron Collider (LHC). Therefore, there are limitations on the possible working points for high-brightness beams.

Both the reduction of the beam blow-up and means to improve the accuracy of emittance measurements at low energy are presented in the chapters of this thesis. Measuring the beam transverse emittance with high precision inevitably causes a better understanding of the emitance growth. In the first part of this study, the emittance blow-up is reduced by re-positioning the LEQs using methods based on numerical optimisation and applying the linear imperfection equations to study the outcome of changes to the current LEQ configuration. This results in multiple possible quadrupole configurations, dependent on the number of allowed re-positionings, which each reduce the emittance blow-up.

The design of the PS does not provide enough space for dispersion suppressors, and the horizontal dispersion function is therefore always larger than zero all along the ring circumference. This imposes that the dispersion function and momentum spread are taken into account in the horizontal emittance calculations, which leads to increased uncertainties in the measured emittance. Therefore, forcing the dispersion function to zero at the horizontal Wire Scanners (WSs) is the second goal of this thesis. For every beam-measurement location, knobs that vary the LEQ strengths are created to move the dispersion from the nominal optics towards zero and back to the nominal optics, causing little distortion to the β-functions along the ring.

Finally, two sources of errors in the K-modulation measurement technique of the β-function used for emittance calculations are studied and minimised so that the β-function at the beam measurement location has a precision of 1%. One error source is the inaccuracy of the Base-Band tune (BBQ) measurement system. The other error source is the limited accuracy of the conversion factor from electric current to quadrupole strength.

This thesis has the following structure. Chapter 2 introduces the reader to theoretical accelerator physics concepts and defines the essential terminology and formulas for understanding the other chapters. A brief overview of the simulation codes used in the studies is given as well. In Chapter 3, the main design of the PS is presented. Afterwards, Chapter 4 sets out to reduce the optics beatings and subsequently the beam blow-up. Chapter 5 devises a method to force dispersion to zero for any PS ring location using the LEQs. Lastly, the errors due to K-modulation are studied in Chapter 6.

2 Accelerator Physics Concepts and Theory

The nominal or ideal trajectory of a particle beam is fixed through the construction of the accelerator. For synchrotrons, the beam needs to be guided through the machine on a circular nominal path. The individual particles inside the beam have a divergence from this path and it is necessary to direct these particles back onto the nominal trajectory or they will eventually touch the beam pipe and become lost. The maximum distance a particle can diverge before it touches the beam pipe is called the mechanical aperture.

The guiding and focusing are achieved through the Lorentz force. For particles with charge e, velocity $\mathbf{v}$ and momentum $\mathbf{p}$ the Lorentz force holds the form

$$\mathbf{F} = e\left(\mathbf{E} + \mathbf{v} \times \mathbf{B}\right) = \dot{\mathbf{p}}, \tag{2.1}$$

where $\mathbf{E}$ and $\mathbf{B}$ are the electric and magnetic fields, respectively. In physical applications a large magnetic field $\mathbf{B}$ can be reached much easier so they are the common field of choice when it comes to bending. Magnetic dipoles handle beam guiding and quadrupoles cause focusing or defocusing depending on their alignment. Higher-order multipoles are used to control effects such as chromaticity and field error compensation, but they have little importance for the studies discussed in this thesis. Nevertheless, they are paramount for successfully operating an actual accelerator. Magnetic fields cannot be used to accelerate the particles in the longitudinal direction, hence electrical fields $\mathbf{E}$ generated in radio frequency (RF) cavities are always utilised for acceleration. A brief introduction to the general solution of Eq. 2.1 as well as to the effect of machine errors is given below. The solution to the Lorentz equation and all its forms depend on the optics of the beam. The derivation of machine errors concludes with equations that relates a modification of the strength of a magnetic element to the change in beam optics. These relations are the foundation of machine optimisation.

Additionally, a common simulation tool to study single-particle optics is introduced. Lastly, a framework to study the importance of space-charge forces is presented that is used for final testing. There is high-quality literature available about the subjects on which the following sections are based [1–10]. The interested reader is referred to these texts for a more in-depth treatment.

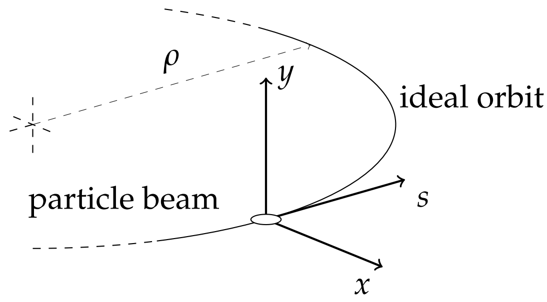

FIGURE 2.1: Left-handed coordinate system used in synchrotrons. x and y characterize the transverse distance from the ideal orbit and s measures the longitudinal distance along it. Figure from [7].

2.1 Linear beam optics

To better understand the Lorentz force, the motion of a particle needs to be described by a Cartesian coordinate system as illustrated in Fig. 2.1. The ideal orbit of an accelerator, as shown in the figure, is the curvature $-\frac{d^2s}{ds^2}$ of the longitudinal distance s determined by the dipolar magnetic elements, or machine lattice. On that note, s is often chosen as the independent variable instead of the time t and the transverse plane is defined by the horizontal coordinate x and vertical coordinate y.
Furthermore, the magnetic field can be expanded near the nominal trajectory for one of the transverse directions and subsequently multiplied by $\frac{e}{p} = \frac{1}{B\rho}$ where the beam rigidity $B\rho$ is a normalisation to connect the magnetic field with the momentum of the beam:

$$\frac{e}{p}B_z(z) = \frac{e}{p}B_{z0} + \frac{e}{p}\frac{dB_z}{dz}z + \ldots \tag{2.2}$$

$$= \frac{1}{\rho} + kz + \ldots \tag{2.3}$$

ρ is the radius of curvature caused by dipoles that guide the beam along the ideal orbit. k defines the strength of beam focusing or defocussing achieved through quadrupoles. Again, the higher order effects are non-linear and are of little importance for the continuation of this thesis.

In this linear approximation the ideal particle moves along the nominal path. Solving Eq. 2.1 in the newly defined coordinate system and using the linear approximation eventually leads to the following inhomogeneous differential equations of motion for particles in accelerators:

$$\begin{gathered} x''(s) + \left(\frac{1}{\rho^2(s)} - k(s)\right)x(s) = \frac{1}{\rho(s)}\frac{\Delta p}{p_0} \\ y''(s) + k(s)y(s) = 0 \end{gathered} \tag{2.4}$$

These are known as Hill's equations and the expression above assumes the absence of vertical guiding fields. Particles in a beam generally have a different momentum from nominal particles. To include this fact, the relative momentum deviation $\frac{\Delta p}{p_0}$ is introduced. Note that in synchrotrons Hill's equations need to satisfy the periodicity conditions $K_z(s) = K_z(s+C)$ with C the circumference of the accelerator and z one of the transverse directions, $K_x(s) = \frac{1}{\rho^2(s)} - k(s)$ and $K_y(s) = k(s)$. The general solution of Eqs. 2.4 in synchrotrons is of the form

$$z(s) = \sqrt{\epsilon_z \beta_z(s)} \cos\left(\mu_z(s) + \mu_{z,0}\right) + \frac{\Delta p}{p_0} D_z(s), \tag{2.5}$$

where the emittance ϵ_z is defined as the area of the phase space ellipse bound by the particle motion in the z-z'-plane, $\beta_z(s)$ is the beta or amplitude function, $\mu_z(s) = \int_0^s \frac{ds}{\beta_z(s)}$ represents the advance in phase space as shown on Fig. 2.2 and is therefore called the phase advance, $\mu_{z,0}$ is the particle's initial oscillation phase and $D_z(s)$ is the dispersion function. Both the β and dispersion functions are periodic with period C. Focusing on the emittance for now, this is a very important property that is not directly quantifiable. A possible workaround, depending on the accelerator optics, is to infer the emittance from beam size measurements. Transverse beam distributions are mostly Gaussian and Eq. 2.5 gives the ability to express the root mean square beam size as

$$\sigma_z(s) = \sqrt{\epsilon_z \beta_z + D_z^2(s) \left(\frac{\Delta p}{p_0}\right)^2}. \tag{2.6}$$

The emittance as defined above is only constant if no acceleration is taking place. Therefore, the normalised emittance ϵ_N is often used because it is energy independent. The relation between ϵ_N and ϵ is

$$\epsilon_N = \beta_{rel} \gamma_{rel} \epsilon, \tag{2.7}$$

where γ_{rel} is the Lorentz factor and β_{rel} is the relativistic velocity.
Coming back to the dispersion, this function is the inhomogeneous solution z_i to the Hill's equation and its effect on z is proportional to $\frac{\Delta p}{p_0}$. Thus, it describes the motion of off-momentum particles. Additionally, the dispersion function is non-zero only if the transverse direction z is curved by ρ. The dispersion can be found using

$$D_z(s) = \frac{\sqrt{\beta_z(s)}}{2 \sin \pi Q_z} \int_s^{s+C} \frac{d\sigma}{\rho(\sigma)} \sqrt{\beta_z(\sigma)} cos\left(\mu_z(\sigma) - \mu_z(s) - \pi Q_z\right). \tag{2.8}$$

Here, the betatron tune Q_z is introduced which is the number of transverse oscillations a particle makes in one revolution around the machine. Alternatively, looking at the phase space ellipse allows the tune to be defined as the accumulated phase advance over one turn.

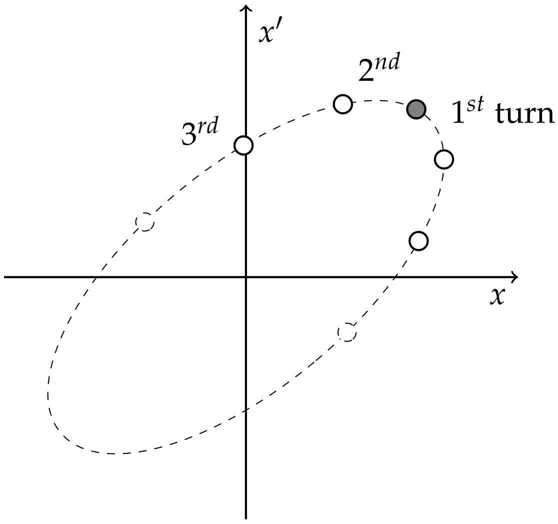

FIGURE 2.2: Horizontal phase space ellipse. After one turn the particle's motion will have changed according to the tune Q_z.

$$Q_z = \frac{1}{2\pi}(\mu_z(C) - \mu_z(0)) = \frac{1}{2\pi}\oint \frac{ds}{\beta(s)} \tag{2.9}$$

$\beta_z(s)$ and $D_z(s)$ are called the linear optics functions. In practice, the optics functions are not known throughout the whole machine but only at few locations. Therefore, a transfer matrix is used, which is a general tool for studying particle motion. Transfer matrices between two locations in a machine can be derived using the general solution of the Hill's equation. Eq. 2.5 leads for on-momentum particles ($\frac{\Delta p}{p_0} = 0$) to

$$\begin{aligned} z(s) &= \sqrt{\epsilon_z \beta_z(s)}\left[\cos\left(\mu_z(s)\right)\cos\left(\mu_{z,0}\right) - \sin\left(\mu_z(s)\right)\sin\left(\mu_{z,0}\right)\right] \\ z'(s) &= -\sqrt{\frac{\epsilon_z}{\beta_z(s)}}[\alpha_z(s)\cos\left(\mu_z(s)\right)\cos\left(\mu_{z,0}\right) - \alpha_z(s)\sin\left(\mu_z(s)\right)\sin\left(\mu_{z,0}\right) \\ &\qquad + \sin\left(\mu_z(s)\right)\cos\left(\mu_{z,0}\right) + \cos\left(\mu_z(s)\right)\sin\left(\mu_{z,0}\right)], \end{aligned} \tag{2.10}$$

with $\alpha_z = -\frac{\beta_z'}{2}$. Defining the initial conditions as $z(0) = z_0$, $z'(0) = z_0'$, $\beta_z(0) = \beta_0$, $\alpha_z(0) = \alpha_0$, and $\mu_z(0) = 0$ one obtains

$$\begin{aligned} cos(\mu_{z,0}) &= \frac{z_0}{\sqrt{\epsilon_z \beta_0}} \\ sin(\mu_{z,0}) &= -\frac{1}{\sqrt{\epsilon_z}}\left(x_0'\sqrt{\beta_0} + \frac{\alpha_0 x_0}{\sqrt{\beta_0}}\right). \end{aligned} \tag{2.11}$$

Substituting this into Eqs. 2.10 allows us to establish the matrix notation.

$$\begin{pmatrix} z(s) \\ z'(s) \end{pmatrix} = M_{0\to s} \begin{pmatrix} z_0 \\ z'_0 \end{pmatrix}, \tag{2.12}$$

with the transfer matrix

$$M_{0\to s} = \begin{pmatrix} \sqrt{\frac{\beta_z(s)}{\beta_0}}(\cos\mu_z(s) + \alpha_0 \sin\mu_z(s)) & \sqrt{\beta_z(s)\beta_0}\sin\mu_z(s) \\ \frac{(\alpha_0-\alpha_z(s))\cos\mu_z(s)-(1+\alpha_0\alpha_z(s))\sin\mu_z(s)}{\sqrt{\beta_z(s)\beta_0}} & \sqrt{\frac{\beta_0}{\beta_z(s)}}(\cos\mu_z(s) - \alpha_0\sin\mu_z(s)) \end{pmatrix}. \tag{2.13}$$

This transfer matrix allows us to define a one-turn transfer matrix which tells how the particle's position in phase space changes over one revolution. The one-turn transfer matrix is

$$M_{0\to C} = \begin{pmatrix} \cos 2\pi Q_z + \alpha_0 \sin 2\pi Q_z & \beta_0 \sin 2\pi Q \\ -\frac{1+\alpha_0^2}{\beta_0}\sin 2\pi Q & \cos 2\pi Q_z - \alpha_0 \sin 2\pi Q_z \end{pmatrix}. \tag{2.14}$$

The one-turn transfer matrix will prove useful when including machine errors in the lattice.

Using the same transfer matrix approach, the propagation of a particle trough a magnetic element can also be calculated. Again, applying Hill's equation 2.4 in case of a horizontally focusing quadrupole ($k < 0$), when there is no bending of the beam ($\frac{1}{\rho} = 0$). One starts from

$$x''(s) - kx(s) = 0, \tag{2.15}$$

where k is constant over the length l of the quadrupole. Considering x_0, x'_0 as initial conditions, this equation leads to

$$\begin{aligned} x(s) &= x_0 \cos\sqrt{|k|}s + \frac{x'_0}{\sqrt{|k|}}\sin\sqrt{|k|}s \\ x'(s) &= -x_0\sqrt{|k|}\sin\sqrt{|k|}s + x'_0\cos\sqrt{|k|}s \end{aligned}. \tag{2.16}$$

From here it is a trivial task to extract the transfer matrix. The technique can be repeated for a defocusing quadrupole and from Eqs. 2.4 it is visible that substituting $|k| = \frac{1}{R^2}$ leads to the transfer matrix of a dipole.

2.2 Linear imperfections

When comparing our theoretical model to reality there will always be discrepancies due to imperfections or errors in the magnetic fields. A perturbation in a dipole field will kick a particle with the same strength every turn. Over several turns the amplitude of the particle will be in range of the aperture leading to particle loss. If the kick does not happen at the same phase on the phase space ellipse turn-by-turn, a stable trajectory is still possible as seen on the second column of Fig. 2.3. A dipolar perturbation will distort the motion by an oscillating wave with the frequency of the tune. Whereas the effect of a quadrupole

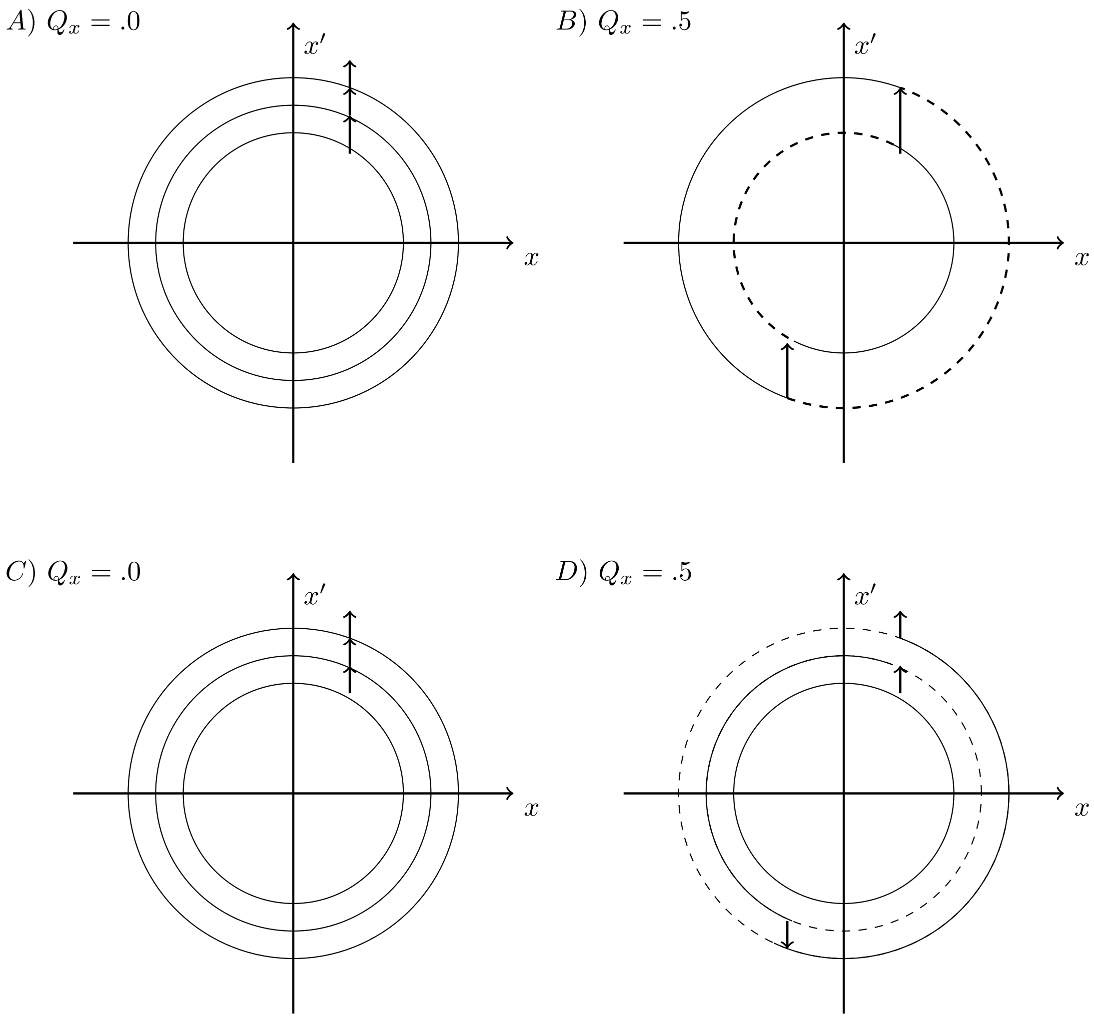

FIGURE 2.3: Illustration of dipolar and quadrupolar resonances in the x-x'-plane. A) and B) are caused by a dipolar error while C) and D) are from quadrupolar errors. A) and C) depict resonances at integer fractional tunes, B) and D) present resonances at half-integer fractional tune. Adapted from [5]

error oscillates with twice the tune. Therefore, at half integer tune values a quadrupole kick will be in alternating directions leading to an increase in particle amplitude that can eventually result in particle loss. These effects are called resonances and higher order magnets will also lead to higher-order resonances. Thus, the choice of transverse tunes or working point (Q_x, Q_y) is important for beam stability.

A quadrupole error δK also translates into a change in optics. For beam operations, these changes must be known. To find an expression for the result of small quadrupole variations on the optics, consider the consequences of a infinitesimally small quadrupole error on the one-turn transfer matrix (Eq. 2.14). The error is found in a short quadrupole section of length ds, sufficiently small that $\cos(\sqrt{k}ds) = 1$ and $\sin(\sqrt{k}ds) = \sqrt{k}ds$. This is the thin element approximation and causes the quadrupole transfer matrix to become without and with error, respectively:

$$m_{quad} = \begin{pmatrix} 1 & ds \\ -k_{quad}(s)ds & 1 \end{pmatrix} \qquad m_{error} = \begin{pmatrix} 1 & ds \\ -(k_{quad}(s) + \delta K)ds & 1 \end{pmatrix} \tag{2.17}$$

Substituting m_{quad} with m_{error} in the one-turn matrix as such

$$M = m_{error} m_{quad}^{-1} M_{0\to C} = \begin{pmatrix} 1 & 0 \\ -\delta K ds & 1 \end{pmatrix} M_{0\to C} \tag{2.18}$$

yields a new one-turn matrix:

$$M = \begin{pmatrix} \cos 2\pi Q + \alpha_0 \sin 2\pi Q & \beta_0 \sin 2\pi Q \\ -\delta K ds \left[\cos 2\pi Q + \alpha_0 \sin 2\pi Q\right] - \frac{1+\alpha_0^2}{\beta_0} \sin 2\pi Q_z & \cos 2\pi Q - (\delta K ds \beta_0 + \alpha_0) \sin 2\pi Q \end{pmatrix} \tag{2.19}$$

Alternatively, the same quadrupolar perturbed one-turn matrix can be obtained by introducing a perturbed frequency $\omega = 2\pi(Q + \delta Q)$ into Eq. 2.14. The tune-shift δQ is caused by the error since quadrupoles account for beam focusing.

$$M^* = \begin{pmatrix} \cos\omega + \alpha_0 \sin\omega & \beta_0 \sin\omega \\ \frac{1+\alpha_0^2}{\beta_0} \sin\omega & \cos\omega - \alpha_0 \sin\omega \end{pmatrix} \tag{2.20}$$

The Matrices M and M^* represent the same physical quantities. Equating the individual matrix elements does not necessarily lead to the desired result since they could use different coordinate systems. The matrix identity that is used is similarity. Two matrices are similar if their traces are the same. Equating the traces gives the relation between δK and δQ.

$$2\cos(2\pi Q) - \delta K ds \beta_0 \sin(2\pi Q) = 2\cos(2\pi(Q + \delta Q)) \tag{2.21}$$

By using the trigonometric relations and the thin lens approximation, this equation unravels to $4\pi\delta Q = \delta K ds \beta_0$. For multiple quadrupole errors distributed

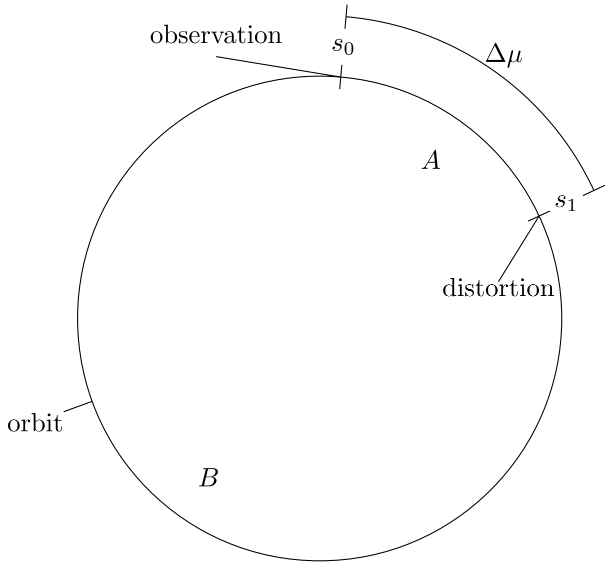

FIGURE 2.4: Calculating the β-distortion at point s_0 due to a quadrupole variation at point s_1 in a synchrotron. Adapted from [1]

over the machine the tune-shift becomes:

$$\delta Q = \frac{1}{4\pi} \oint \delta k(s)\beta(s)ds \tag{2.22}$$

Note, this equation only holds true when the quadrupole errors $\delta k(s)$ are small.

While the tune is a general attribute of a magnetic lattice, a quadrupole error modifies the focusing properties at all longitudinal positions s of the lattice and thus the optics functions along the whole machine. Therefore, we aim at calculating the modified β function. As such, the β-distortion at point s_0 in the lattice from the quadrupole error, again infinitesimally small, at point s_1 is examined. Let the phase difference between the two points be $\Delta\mu$. Use Eq. 2.13 to describe the machine between s_0 and s_1 as matrix **A**. Similarly, let matrix **B** be the transformation between point s_1 and s_0, as seen in Fig. 2.4.

To make the following derivation more clear, the unperturbed one-turn matrix is written as $M = \begin{pmatrix} m_{11} & m_{12} \\ m_{21} & m_{22} \end{pmatrix} = \mathbf{B}.\mathbf{A}$ and the perturbed matrix is $M^* = \begin{pmatrix} m^*_{11} & m^*_{12} \\ m^*_{21} & m^*_{22} \end{pmatrix}$. It suffices to only consider matrix elements m_{12} and m^*_{12} to get the β-distortion. Looking solely at the one-turn matrix we expect these matrix elements to respectively have the following values:

$$m_{12} = \beta_0 \sin 2\pi Q \qquad m^*_{12} = (\beta_0 + \delta\beta) \sin 2\pi(Q + \delta Q) \tag{2.23}$$

Where $\beta_0 = \beta(s_0)$. Matrix element m^*_{12} is also obtainable through the following matrix product:

$$\begin{pmatrix} m^*_{11} & m^*_{12} \\ m^*_{21} & m^*_{22} \end{pmatrix} = \mathbf{B}. \begin{pmatrix} 1 & 0 \\ -\delta k ds & 1 \end{pmatrix} .\mathbf{A} \tag{2.24}$$

$$\begin{aligned} m_{12}^* &= m_{12} - a_{12}b_{12}\delta k ds \\ &= \beta_0 \sin 2\pi Q - a_{12}b_{12}\delta k ds \end{aligned} \tag{2.25}$$

Setting both expression equal to each other, using the thin lens approximation again and neglecting second order terms in δk, gives:

$$\delta\beta = -\frac{1}{2\sin 2\pi Q}\left[2a_{12}b_{12}\delta k ds + 2\pi\delta Q\beta_0 cos 2\pi Q\right] \tag{2.26}$$

Filling in the following relations and using the tune-shift equation (Eq. 2.22) from the previous paragraph:

$$a_{12} = \sqrt{\beta_0\beta(s_1)} sin\Delta\mu \tag{2.27}$$

$$b_{12} = \sqrt{\beta_0\beta(s_1)} sin(2\pi Q - \Delta\mu) \tag{2.28}$$

It follows that the β-distortion of a single quadrupole error at location s_1 is

$$\delta\beta = -\frac{\beta_0\beta(s_1)}{2\sin 2\pi Q}\cos(2\Delta\mu - 2\pi Q)\delta k ds. \tag{2.29}$$

Expanding this solution to the β-beating equation for distributed errors around the machine

$$\Delta\beta(s) = -\frac{\beta(s)}{2\sin 2\pi Q}\int_s^{s+C} \beta(\sigma)\delta k(\sigma)\cos(2(\mu(\sigma) - \mu(s)) - 2\pi Q) d\sigma. \tag{2.30}$$

The presence of betatronic resonances is clearly visible in the β-beating equation as $\frac{1}{sin 2\pi Q}$ blows up if Q has an integer or half-integer value. Using the modified β function in the definition of phase advance also allows for the perturbed phase advance to be found. Resulting in $\mu^*(s) = \int_0^s \frac{1}{\beta(s)+\Delta\beta(s)}$. For small quadrupole errors the perturbation to the phase advance is small enough that it can be neglected in the β-beating equation. However, the new phase advance needs to be included for the perturbed dispersion function, as shown in Fig. 2.5. The new dispersion function is calculated by using the perturbed β-function, phase advance and tune in Eq. 2.8.

2.3 MAD-X

The Methodical Accelerator Design (MAD)-X program [11–13] is the main tool for designing and optimizing accelerators and other lattices at CERN. MAD-X allows the user to investigate the optics of a sequence of magnetic elements and can solve various other problems on such sequences. To attain a sequence, each element needs to be defined by its type (dipole, quadrupole, RF cavity, etc.) and its geometric properties (positioning, length, etc.). Subsequently, the magnetic strengths of the active elements can be set. Note that at any point, elements can be moved, removed, redefined, etc. When the desired lattice is correctly installed, the optical parameters can be calculated. If the lattice has

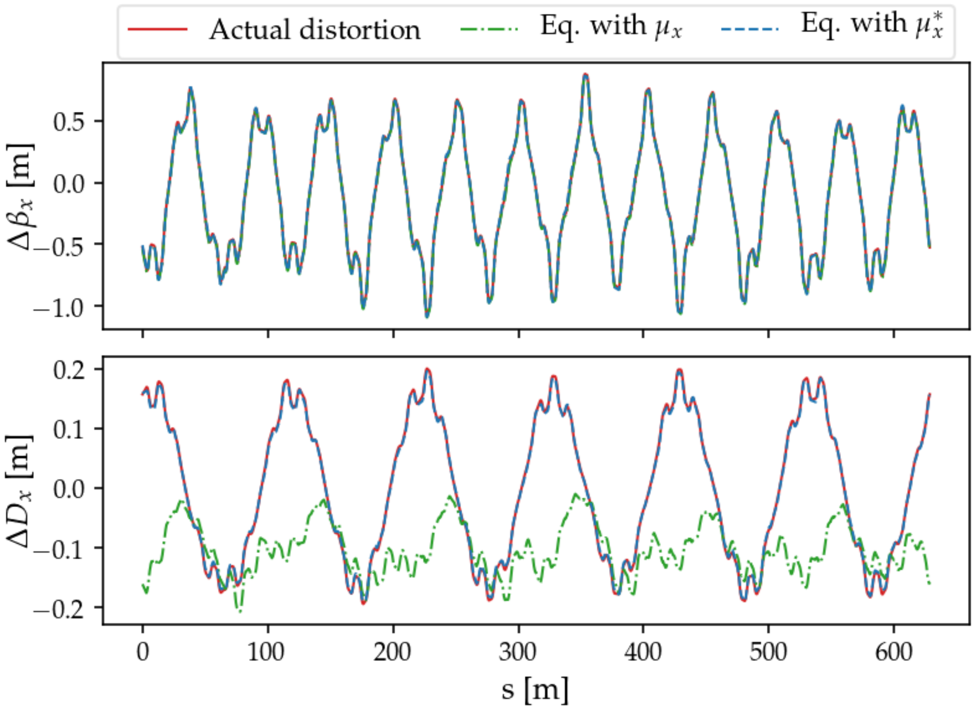

FIGURE 2.5: Comparison of the horizontal β-beating (Eq. 2.30) and the horizontal dispersion beating (Eq. 2.8) with and without using the perturbed phase advance μ_x^*. Clearly showing that the updated phase advance needs to be considered in further calculations.

a desired property, such as a certain working point (Q_x, Q_y), MAD-X is able to match the tunes accordingly. This is done by varying other properties of the machine using different available matching methods. It is also possible to include magnetic errors on the lattice elements and evaluate their effect on the particle motion.

Every CERN accelerator has been modelled, benchmarked and updated after experimental measurements [14]. Therefore, MAD-X is a suitable tool for the studies in the following chapters.

2.4 Space-charge simulation framework

A charged particle beam is a collection of moving charged particles. Apart from the external electromagnetic fields, the beam itself also produces electromagnetic fields. The effects of the electric charge of the beam are divided in the direct and indirect space-charge effects. The electromagnetic field induced by the particles that trail behind the beam are called wakefields. The interaction of the beam with the conductivity of the smooth beam pipe are indirect space-charge effects and the generated effects of the beam's interaction with itself are direct space-charge effects.

Even though a special version of MAD-X is able to consider space-charge effects, MAD-X is intended as as code for single-particle calculations. Fortunately, there has recently been a study that successfully benchmarked the simulated direct space-charge effects to an experimental measurement campaign performed in the PS [15–17]. The used simulation framework essentially simulates a MAD-X sequence with direct space-charge forces, but neglects the indirect space-charge forces. The framework is written using PyORBIT [18]. PyORBIT allows to track a particle bunch through a magnetic sequence with frequent space-charge nodes, where the beam distribution is calculated and the particles receive a coulomb kick dependent on this distribution. Hereby, it enables one to test changes in the PS magnetic lattice with the inclusion of space-charge effects. The sequence that is simulated in the initial study is the PS magnetic lattice of 2018 that produces proton beams destined for the LHC. Any other relevant characteristics of the space-charge framework will be explained in later chapters. The implementation of the MAD-X or space-charge code and discussions on the applied models are omitted since code development is not the objective of this thesis.

3 The CERN Proton Synchrotron

The PS has had many purposes over its lifetime. Initially designed as the world's first accelerator based on the alternating-gradient focusing principle and accelerating protons to its operational energy of 26 GeV in November 1959, the PS has since produced beams for many fixed target experiments and has served as a pre-accelerator to numerous other CERN accelerators, e.g. the Super Proton Synchotron (SPS), the Large Electron-Positron (LEP) collider, the LHC. Today, the versatility and reliability of the PS is an essential part of CERN operations. In what follows, an overview is given of the main components of the PS [19–21].

3.1 The design of the PS

The accelerator is made up of 100 quasi-identical combined-function Magnet Units (MUs) installed around a $2\pi \times 100$ m-circumference ring. A MU consists of a focusing and defocusing half-unit. Between the MUs there are 100 straight drift sections (SSs) where extra devices can be placed, like beam measurement devices and auxiliary magnets. Injection and extraction also occurs in the SSs. The MUs and SSs together cause a recurring 'FOFDOD' pattern where F stands for focusing magnets, D for defocusing magnets and O for free space, i.e. without magnetic field, representing the SSs.

The previous chapter states that the working point is an important parameter for beam stability. There are two different ways of controlling the working point, i.e. the LEQs and the pole face windings (PFWs) [24, 25]. On the one

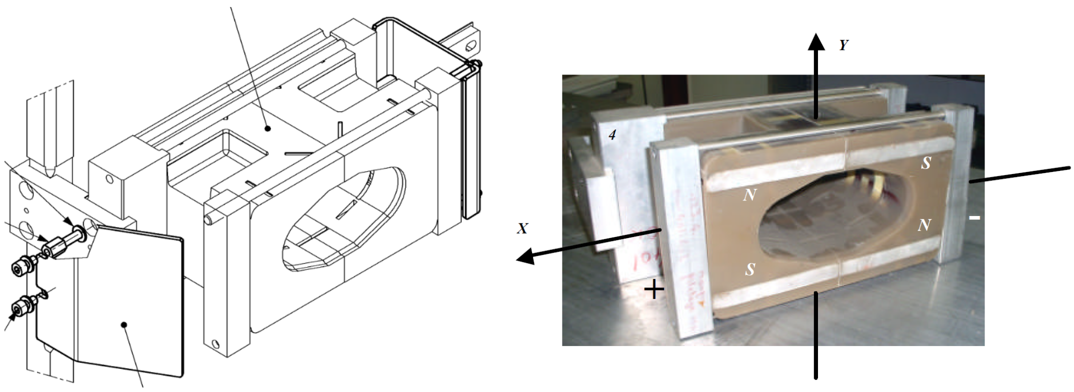

FIGURE 3.1: Drawing and foto of a type 1 PS LEQ. Drawing from [22] and foto from [23].

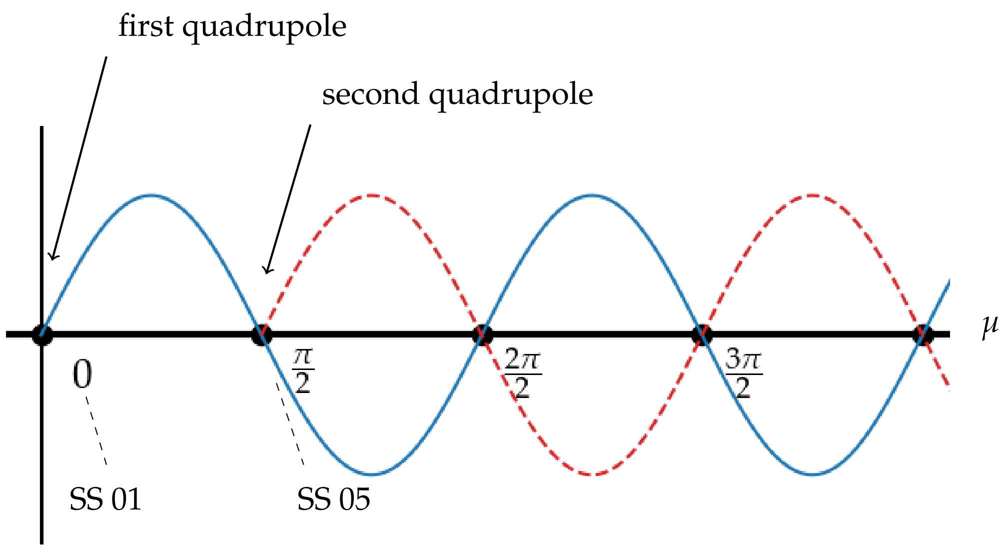

FIGURE 3.2: Propagation and cancellation of β variation from two consecutive LEQs with $\Delta\mu = \frac{\pi}{2}$ between them, in the PS.

hand the PFWs are extra magnetic elements on top of the hundred combined-function magnetic poles that add extra control to quadrupolar, sextupolar and octupolar field components. They are smoothly distributed across the ring. On the other hand, the LEQs are used to control the transverse tunes from injection energy to ≈3.5 GeV. Before the Long Shutdown 2 (LS2) injection took place at 1.4 GeV kinetic energy and the injection energy has been raised to 2 GeV during LS2 [26]. LEQs are limited in strength so at higher energies the PFWs are used to control the working point. There are 2 types of LEQ used in the PS depending on the available space. Type 1 (Fig. 3.1) is the most common and has an integrated magnetic gradient of 35.37 mT at 6A. Type 2 has larger mechanical aperture and hence a reduced integrated magnetic gradient at 6A of 25.99mT. Both can be operated from -20 A to 20 A [27]. Note that the beam rigidity needs to be taken into account when going to magnetic strength used in simulations. Historically there were 50 LEQs installed in the PS [23]. They came in focusing and defocusing pairs in successive SSs every four sections. The symmetry of the quadrupole placements allowed the optics functions to stay smooth even for large tune deviations from the bare machine working point. Since the design tune of the PS was 6.25, two quadrupoles of the same type would be $\frac{\pi}{2}$ apart from each other in phase advance. Looking at Eqs. 2.30 tells us that a betatronic wave travels through the machine at $2 \times Q$. Hence, the beating induced by two consecutive focusing quadrupoles would compensate each other as shown in Fig. 3.2. Unfortunately, over the years some LEQs were removed or moved to make place for other installations. Currently, there are 40 LEQs installed in the PS lattice that don't satisfy any symmetry relations. This loss of symmetry is clearly visible in the beta and dispersion functions when the working point is moved closer to either the horizontal or vertical integer resonance or both, as shown in Fig. 3.3.

The combined-function MUs only guide the beam in the horizontal direction and there is no vertical bending magnet in the PS. Consequently, the vertical dispersion is zero along the whole ring. The non-zero horizontal dispersion was not an issue when the PS was built. At that time, the intensity of the beam was the main priority and the PS ring was not provided with enough space for dispersion suppressors. At the present time and especially considering high-brightness beams for the LHC, the emittance is much more of a concern and the presence of horizontal dispersion makes accurate emittance measurements difficult.

The beam size, and therefore beam emittance, in the PS is measured using a WS, Secondary Electron Emission grids (SEM-grid) or Beam Gas Ionization monitors (BGI)[28–32]. BGIs rely on the residual gas particles, present in the vacuum pipe, and their collision with the beam to generate secondary particles. The secondaries are then guided by an electric field outside of the beam path towards a detector, where the beam distribution is reconstructed. A WS measures the beam size by rapidly moving a perpendicularly stretched wire through the beam. Secondary particles produced by this interaction hit a scintillator and the signal is amplified by a photo multiplier, which together act as a detector. The output, sampled with the wire's position, is the projected beam profile. Before LS2, the WSs in the PS looked similar to Fig. 3.4. Some of the moving parts of the WS were placed outside the vacuum chamber of the beam, leading to an increased probability for vacuum leaks after extensive use of the devices. During LS2, the WSs were upgraded in the framework of the LHC Injectors Upgrade (LIU) project [26]. The moving parts of the upgraded WSs are placed inside of the vacuum chamber and therefore increase reliability of the scanners. A schematic overview of an upgraded WS is presented in Fig. 3.5

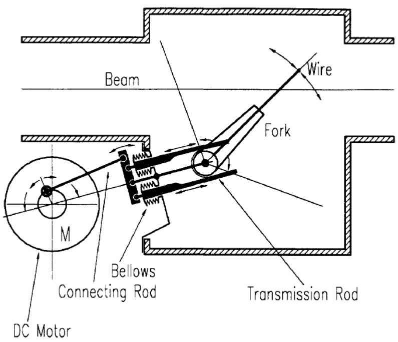

FIGURE 3.4: Schematic view of the WS mechanism. Figure from [30].

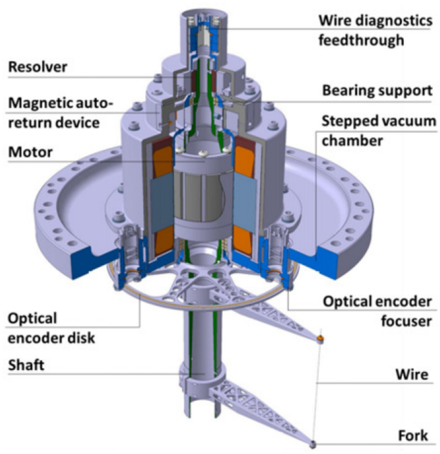

FIGURE 3.5: Upgraded WS developed in the framework of the LIU project. Figure from [31].

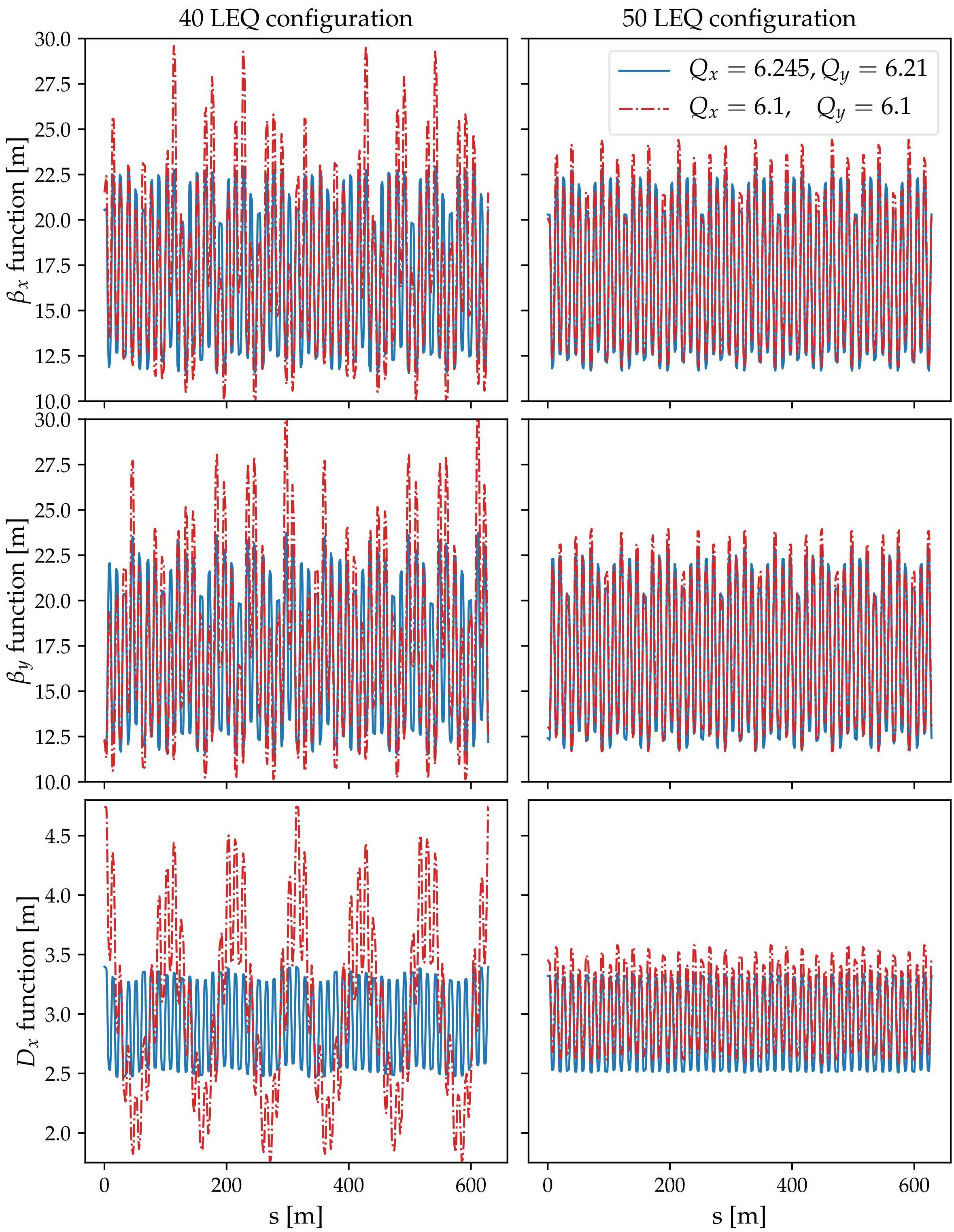

FIGURE 3.3: β and dispersion beating comparison between the current 40 LEQ lattice and the original 50 LEQ configuration. The optics distortion becomes prevalent when the working point is moved to the integer tunes at (6.0,6.0).

SEM-grids also detect secondary particles caused by the interaction of wires with the beam, but here an array of wires is placed in the beam path. The secondary electron current caused by the interaction is then measured and sampled to form a beam distribution. For beams above 1 GeV kinetic energy, the relative energy loss due to the interaction is negligible. In the following chapters an instrumentation in a specific SS will be referred to as the abbreviation of the instrument followed by the number of the SS, for example an LEQ in SS 65 is referred to as LEQ 65.

4 Optics Optimisation

The deviation from the nominal optics when the working point is moved away from its nominal value is called β- and dispersion-beating. Numerically, β-beating is defined as $\frac{\Delta\beta}{\beta}$. Dispersion beating is defined in the same way and both are presented on Fig. 4.1.

The experimental measurements on which the initial space-charge study was based (see also Chapter 2.4), found a clear emittance blow-up when the beam is brought closer to the integer tunes using the LEQs, as presented on Fig. 4.2. The space-charge study considered the source of beam blow-up and was able to replicate the emittance increase when using the LEQs to move the working point. Fig. 4.3 displays the similarities of the simulation and the experimental measurements and Fig. 4.4 shows that using the PFWs does not cause the same blow-up.

These results led to the conclusion that the large optics beating excites the half-integer resonance at a tune of 6.0. In this chapter, possible re-positioning of the installed LEQs is studied and tested to reduce optics beatings and therefore the emittance growth. This problem will first be handled using single-particle calculations to find new quadrupole configurations. Afterwards, the configurations are tested using space-charge simulations. To accomplish this, all straight sections, where the installation of an LEQ at the beginning of the MUs were possible, had to be found. This was done by using the extensive PS engineering documentation and by looking at the actual machine. 12 available SSs were found on top of the 40 sections that already have an LEQ installed. These available SSs are presented in Fig. 4.5. Some of the currently used straight sections have enough free space for an additional LEQ to be installed. These additional possibilities are considered in the calculations.

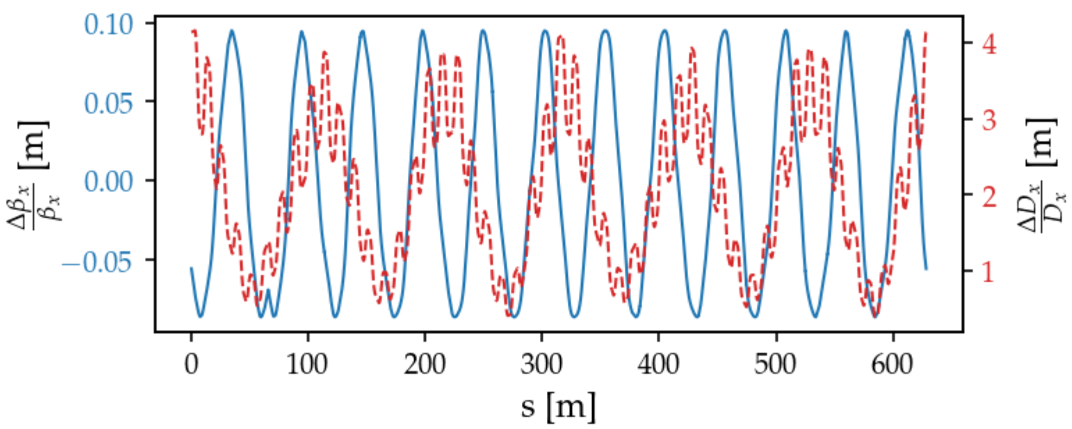

FIGURE 4.1: β_x and horizontal dispersion-beating from a 5 mT/m integrated quadrupole strength variation in LEQ 10.

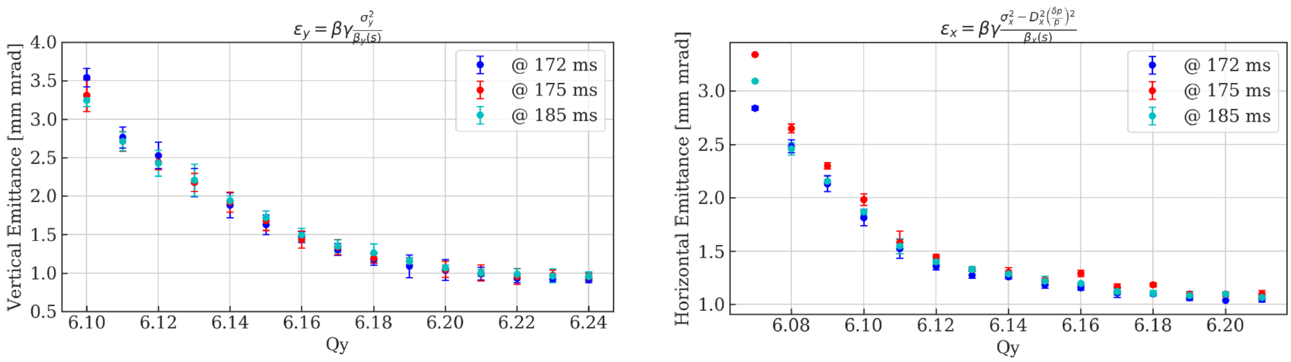

FIGURE 4.2: Experimental emittance measurements while the working point ($Q_x = 6.21$) is moved with the LEQs. Figure from [16].

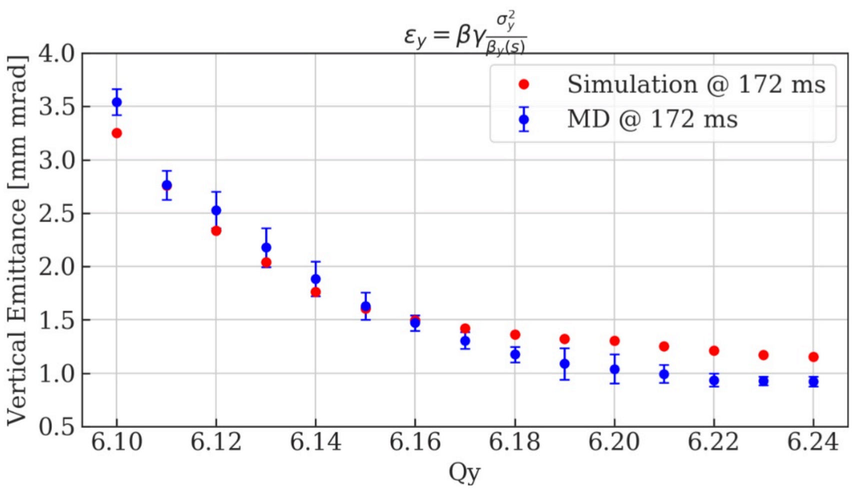

FIGURE 4.3: Comparison of the experimental emittance measurements and a replication from space-charge simulations while the working point ($Q_x = 6.21$) is moved with the LEQs. Figure from [16].

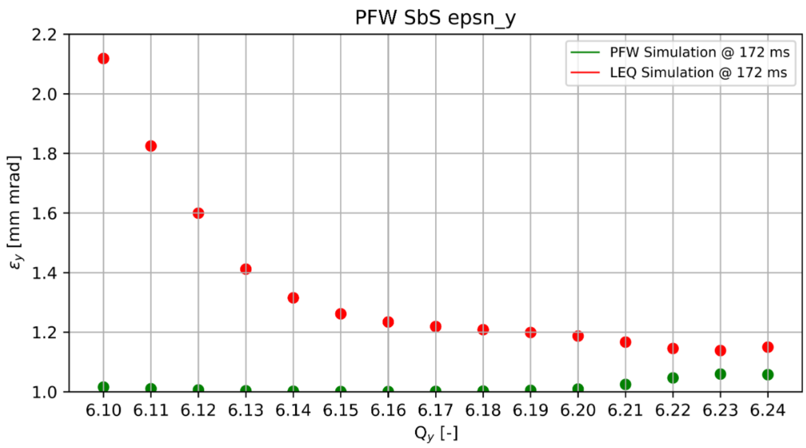

FIGURE 4.4: Replication of the experimental emittance measurements using space-charge simulations while the working point ($Q_x = 6.10$) is moved by either the LEQs or the PFWs. Figure from [16].

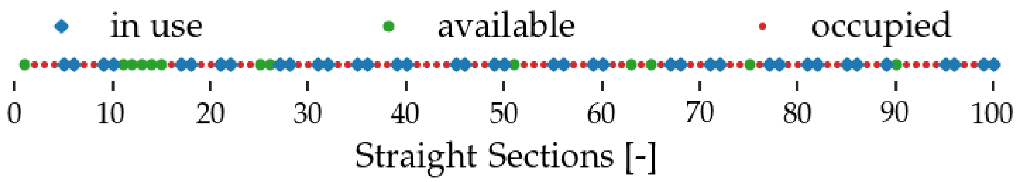

FIGURE 4.5: Availability of the PS straight sections. The blue markers represent the currently installed LEQs, green are the straight sections that can hold an LEQ and the red markers are unavailable sections.

The following single-particle studies are done on a MAD-X PS lattice with a proton beam that replicates a 2018 measurement of the bare machine [33]. The tune and chromaticity of the MAD-X lattice is matched to a reference measurement to give identical numbers when the LEQs are turned off. The LEQs are able to be individually powered, but for this study all the LEQs that focus on the same plane are used with the same strength, which is equivalent to how the LEQs are used in operation. Potential quadrupole configurations that reduce optics beating will then be tested using the space-charge framework.

4.1 Optimisation algorithm

The available SSs don't possess an exploitable symmetry since they are randomly spread along the ring. Therefore, a new method had to be developed to select quadrupole placements. A numerical optimisation algorithm is tested in this section [34, 35]. A general formulation, following the conventions from [35], of a constrained optimisation problem can be written as:

$$\underset{x \in \mathbb{R}^n}{\text{minimise}}\ \xi(x) \qquad \text{subject to } g_i(x) \leq 0, \quad i = 1, 2, \ldots, m,$$

where ξ and g_i are smooth, real-valued functions on a subset of $\mathbb{R}^n$. They are, respectively, called the objective function and constraints. A constrained optimisation algorithm will iteratively vary the optimisation variables x to test the objective function in the feasible region, which is the set of points satisfying all constraints, using a method specific to the solver to approach the optimal point or solution. The optics beating problem can be converted to a constrained optimisation problem, as illustrated in Fig. 4.6, by using the following concepts:

- Let the optimisation variable x_j be the position of quadrupole j with $j = 1, 2, \ldots, 40$. The positions are allowed to continuously vary over the circumference of the whole machine. This also defines the constraints as $0 \leq x \leq C$, with C being the circumference of the PS. Every optimisation step will begin with a bare PS lattice where all LEQs are removed. Then, the solver varies the optimisation variables resulting in a list of 40 positions. Quadrupoles cannot yet be installed in the PS lattice at these positions . First, every location needs to be moved to the nearest available SS. After relocating, the resulting 40 locations become a valid quadrupole

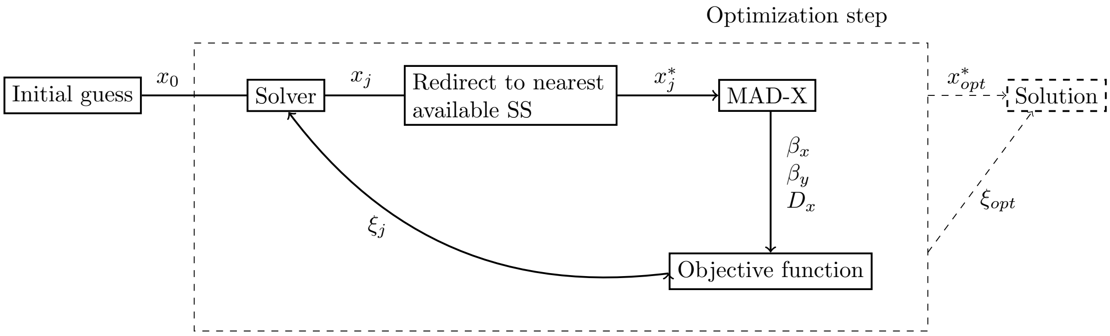

FIGURE 4.6: Schematic overview of the optimisation algorithm.

configuration. In the simulations, the LEQs are then installed at the locations according to the obtained configuration.

- The objective function will need to convert the optics beating into a real number. Optics beating becomes more prevalent if the working point lays near the integer resonance. To enhance the optics beating, the working point of the PS will first be moved to (6.1, 6.1) using the LEQs. This is done with the matching module of MAD-X. A possible objective function is
$$\xi(x) = \frac{\sigma(\beta_x) + \sigma(\beta_y) + \sigma(D_x)}{3}, \tag{4.1}$$
with $\sigma(f)$ the standard deviation of the function between brackets. This objective function definition relies on the fact that the beatings are essentially large variations in the optics functions. These large variations in a sample translate into increased standard deviation. The objective function $\xi(x)$ is tested by comparing the ξ-value of the ideal 50 LEQ-configuration and the ξ-value of the current 40 LEQ-configuration, with $\Delta\xi$ being the difference between the two. The results are shown in Fig. 4.7. The figure shows a clear increase for the current lattice compared to the ideal configuration. For the continuation of this study a normalised $\xi^* = \frac{\xi}{\xi_0}$ is used where ξ_0 corresponds to the bare machine lattice where the LEQ strengths are set to zero and hence no optics beating is present. ξ^* of the current lattice is equal to 1.2460.

- Before deciding on a publicly available solver of optimisation problems, note that the choice of optimisation variables x causes the objective function to be discrete. This is due to the relocation-step causing the objective variables to have only discrete values, which are the positions of the available straight section. Thus, the objective function jumps between quadrupole configurations with different ξ-values, as shown in Fig. 4.8. Because of this discretization, the optimisation problem is ill-defined and potentially causes problems for solvers that should be able to deal with this type of problem. Therefore, multiple solvers are tested: Py-BOBYQA [36], Bayesian Optimisation [37], ZOOpt [38] and Scipy.optimize [39]. One test where each solver begins from a random initial configuration is shown

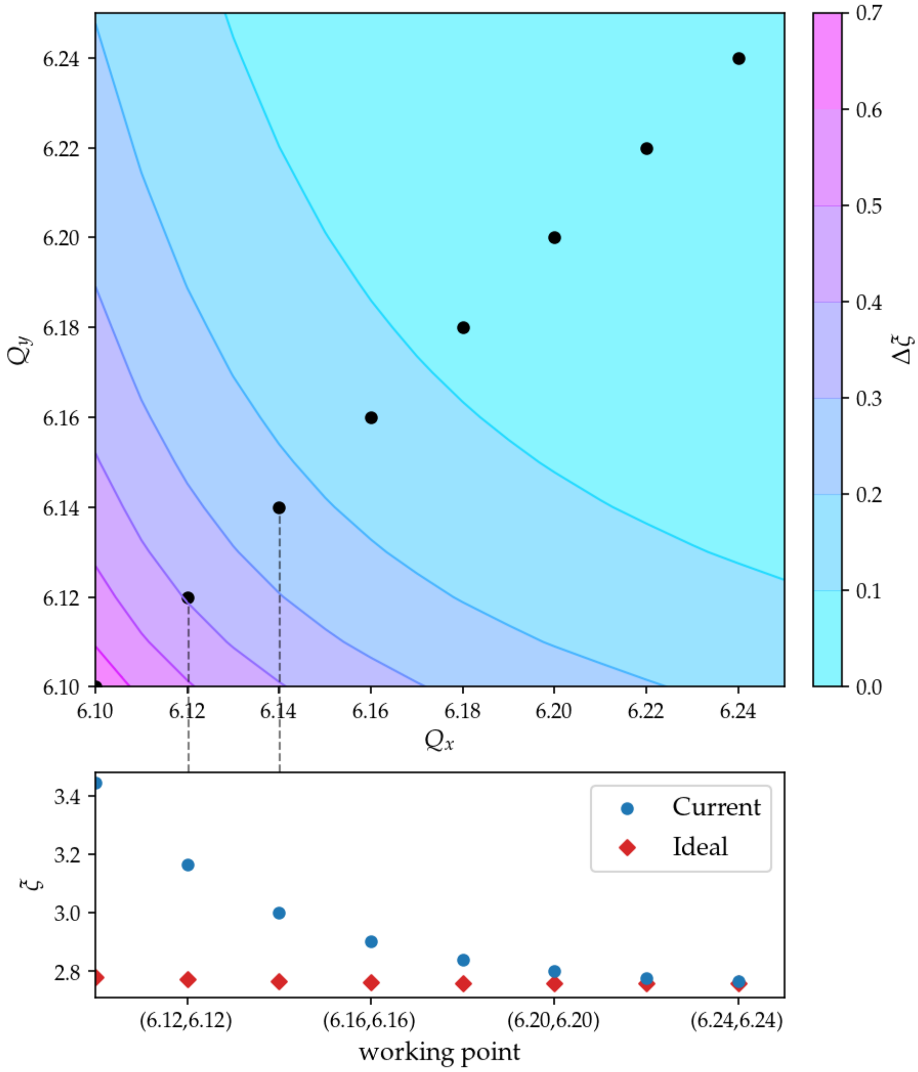

FIGURE 4.7: ξ for both current and ideal LEQ configurations when the working point is moved closer to the integer resonance, with $\Delta\xi$ being the difference between both configurations.

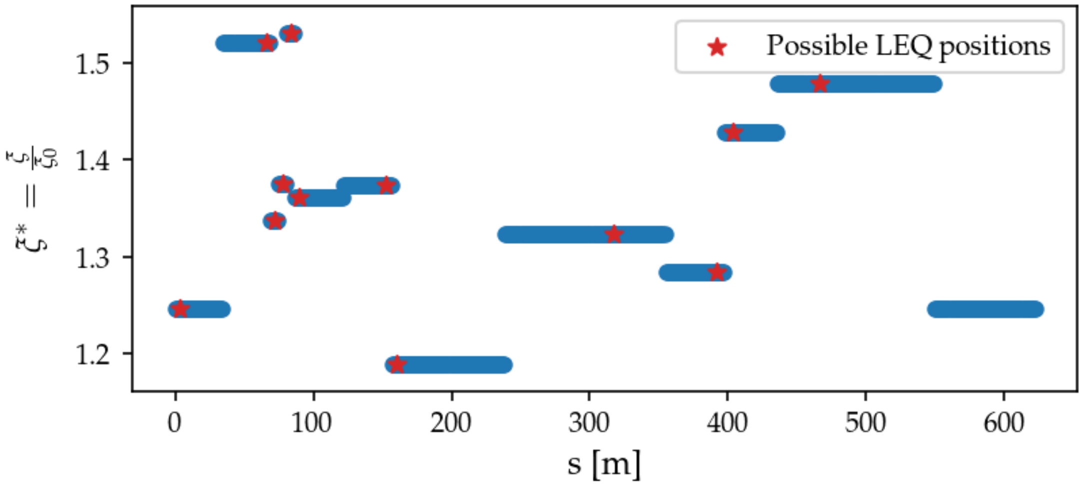

FIGURE 4.8: Projection of ξ on a plane where only one quadrupole is moved across the current lattice. The objective function changes value 12 times since there are 12 available SSs. Possible duplicate positions are not included in this plot.

in Fig. 4.9. The ZOOpt-package is chosen since it would consequently perform better than the other solvers for this specific problem. ZOOpt stands for zeroth-order optimisation (a.k.a. derivative-free optimisation/black-box optimisation). It relies mostly on taking samples of the search space and is therefore suitable for optimising functions that are only testable, as in the case presented here.

With the optimisation framework fully defined, it was run many times each with a different initial guess. The amount of optimisation iterations and optimisation steps was limited due to computing time required for one optimisation step (≈ 2.5 s). Some of the iterations are shown on Fig. 4.10. From this, one can conclude that the result of one iteration depends heavily on the initial guess. Therefore, it must be assumed that only local minima are found. However, for these local minima ξ^* has already been improved in most cases.

Only the quadrupole configuration with the lowest objective function, i.e. $\xi^* = 1.1037$, was investigated in the context of emittance blow-up. Since this configuration was found using the optimisation algorithm, we'll name it the optimised lattice. There would be 10 changes needed to go from the current lattice to the optimised lattice: removing the quadrupoles in SS 55, 72, 95, 99, 100 and installing quadrupoles in SS 13, 14, 25, 26, 63. The current and optimised optics are shown in Fig. 4.11. A clear improvement of the peak to peak values are seen in the horizontal β-function and a smaller improvement in the vertical β-function. The optimised dispersion function shows great improvement over the first half of the lattice and a slight deterioration in the latter half. This global enhancement, but local worsening in the dispersion function is an outcome of the objective function formulation, which conveys that there is room for improvement.

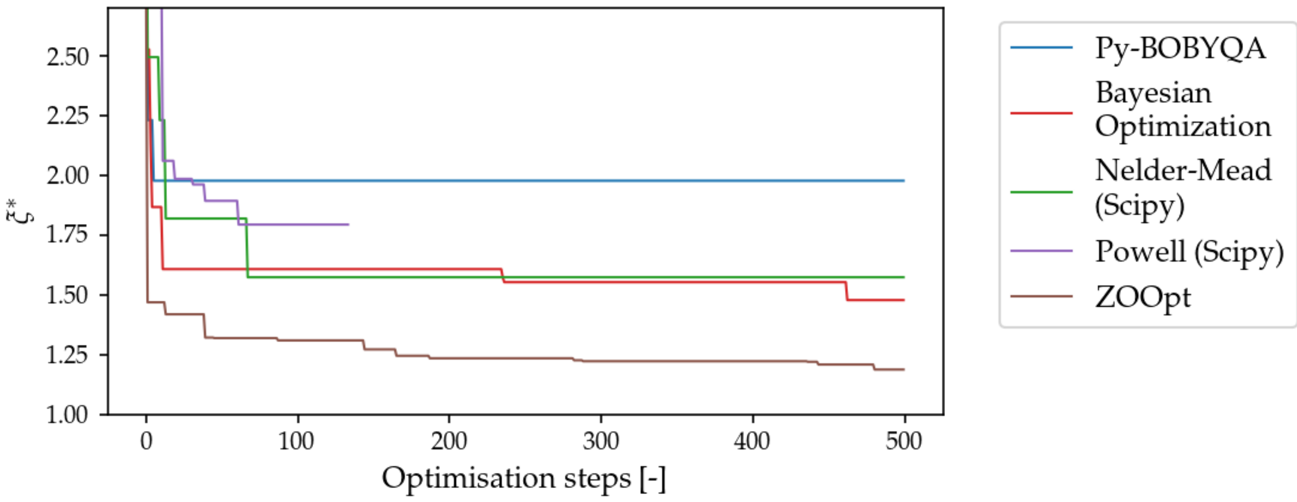

FIGURE 4.9: Progress of an optimisation algorithm iteration using different solvers starting from a random initial quadrupole configuration.

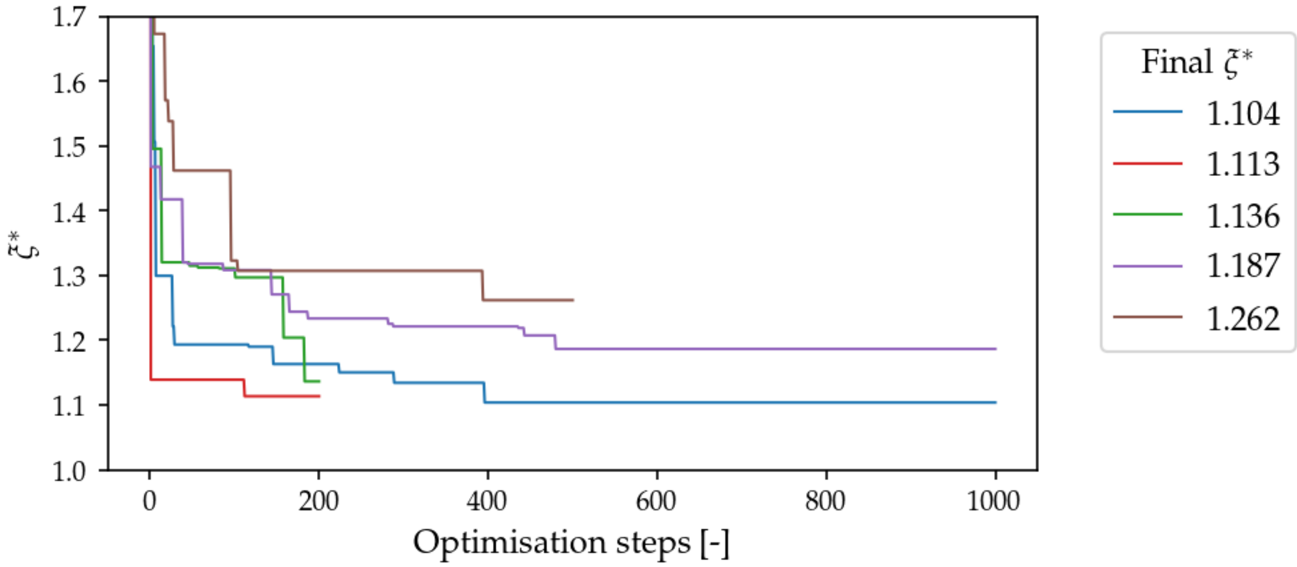

FIGURE 4.10: A selection of optimisation iterations using the ZOOpt-package each with different initial quadrupole configurations.

While the optimised lattice does results in improvements to the optics beatings, introducing 10 changes to the current quadrupole configuration is very challenging for an experimental test setup. Additionally, this method is unfit to explicitly look for configurations where less changes are made, due to the way the optimisation problem is designed.

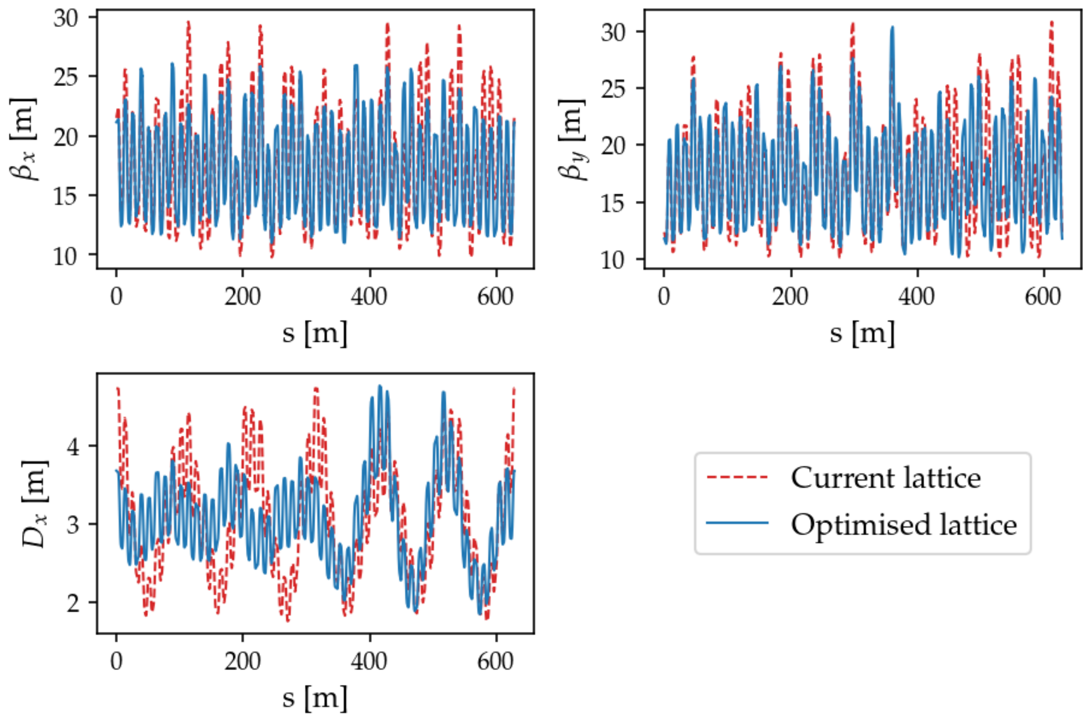

FIGURE 4.11: β_x, β_y and D_x functions of the current LEQ configuration and optimised configuration at working point (6.1,6.1).

4.2 Single quadrupole addition or removal

Keeping the results from the previous section in mind, a new approach is required to find an easily testable quadrupole configuration. This process is started by examining whether a better β- and dispersion-beating is achievable by making a single change to the current operational lattice. With Eqs. 2.8, 2.22 and 2.30 from Chapter 2, it is possible to predict the optical perturbations due to a quadrupole error or small change in quadrupole strength. Taking into account the approximation made in that chapter, testing is needed to see if these equations can be used to accurately calculate the outcome of removing or adding an LEQ. The aforementioned equations are repeated here for clarity:

$$\begin{aligned}
\Delta\beta(s) &= -\frac{\beta(s)}{2\sin 2\pi Q}\int_s^{s+C}\beta(\sigma)\Delta k(\sigma)\cos(2(\mu(\sigma)-\mu(s))-2\pi Q)d\sigma \\
\Delta Q &= \frac{1}{4\pi}\oint \Delta k(s)\beta(s)ds \\
D(s)+\Delta D(s) &= \frac{\sqrt{\beta(s)+\Delta\beta(s)}}{2\sin\pi(Q+\Delta Q)}\int_s^{s+C}\frac{1}{R(\sigma)}\sqrt{\beta(\sigma)+\Delta\beta(\sigma)} \\
&\qquad cos\left[(\mu(\sigma)+\Delta\mu(\sigma))-(\mu(s)+\Delta\mu(s))-\pi(Q+\Delta Q)\right]d\sigma
\end{aligned}$$

In Fig. 4.12 the results of applying these formulas in the four cases of adding or removing a focusing or defocusing LEQ are shown. The figure also shows that attempting to make 2 changes without updating the optics between every change causes the approximations to become invalid due to the large strengths.

The value of ξ^* is predicted for adding an LEQ where possible and removing an LEQ where possible, resulting in Fig. 4.13, on which there are many improvements to the current lattice visible. Note that one dot on the figure represent one change in the lattice, so the red dots would result in a quadrupole configuration with 39 LEQs and the green dots result in configuration with 41 LEQs. The goal is to find a quadrupole configuration of 40 LEQs or less to be able to easily test it in the machine by virtually disconnecting one quadrupole in the control system. Therefore, the green dots that represent adding an LEQ are not considered as viable options, but they are added on the figure to fully illustrate the method. Every dot on Fig. 4.13 represents a new quadrupole configuration with a single change. By selecting the configurations with the smallest ξ^*-values and repeating again the process of testing the effect of a single change of a quadrupole, they will lead to quadrupole configurations with two changes. This process can be repeated in a branch-like structure. The branching depth will equal the number of changes to the initial magnetic lattice. Consider that this method would give the optimal configuration for a specific depth if the number of branches is equal to the number of possible changes. However, depth m with n branches would require n^m calculations. The number of calculations gravely restricts this method. This is especially true since the optics of each configuration needs to be updated using MAD-X for every branching depth as Fig. 4.12 shows that changing 2 LEQs leads to large errors.

An optimal quadrupole configuration was already found in the previous section so this new branching method is used to search for configurations with 5 changes or less with 9 branches at every depth. The result of the branching method is shown on Fig. 4.14. The changes leading to the best configuration at every depth as well as their ξ^* are recorded in Table 4.1 and their optics in comparison to the initial optics are depicted in Figs. 4.15 and 4.16. Every configuration visually reduces the peak-to-peak ratios and thus improves the optics beatings. However, ξ^* decreases slowly over the number of changes. The lattice with only one change, where only LEQ 90 is removed, appears to be the most interesting since this change is easily made to the current lattice and can hence be easily tested in the machine. As the 2 changes lattice shows a higher ξ^* value than the 1 change lattice it is removed from further testing.

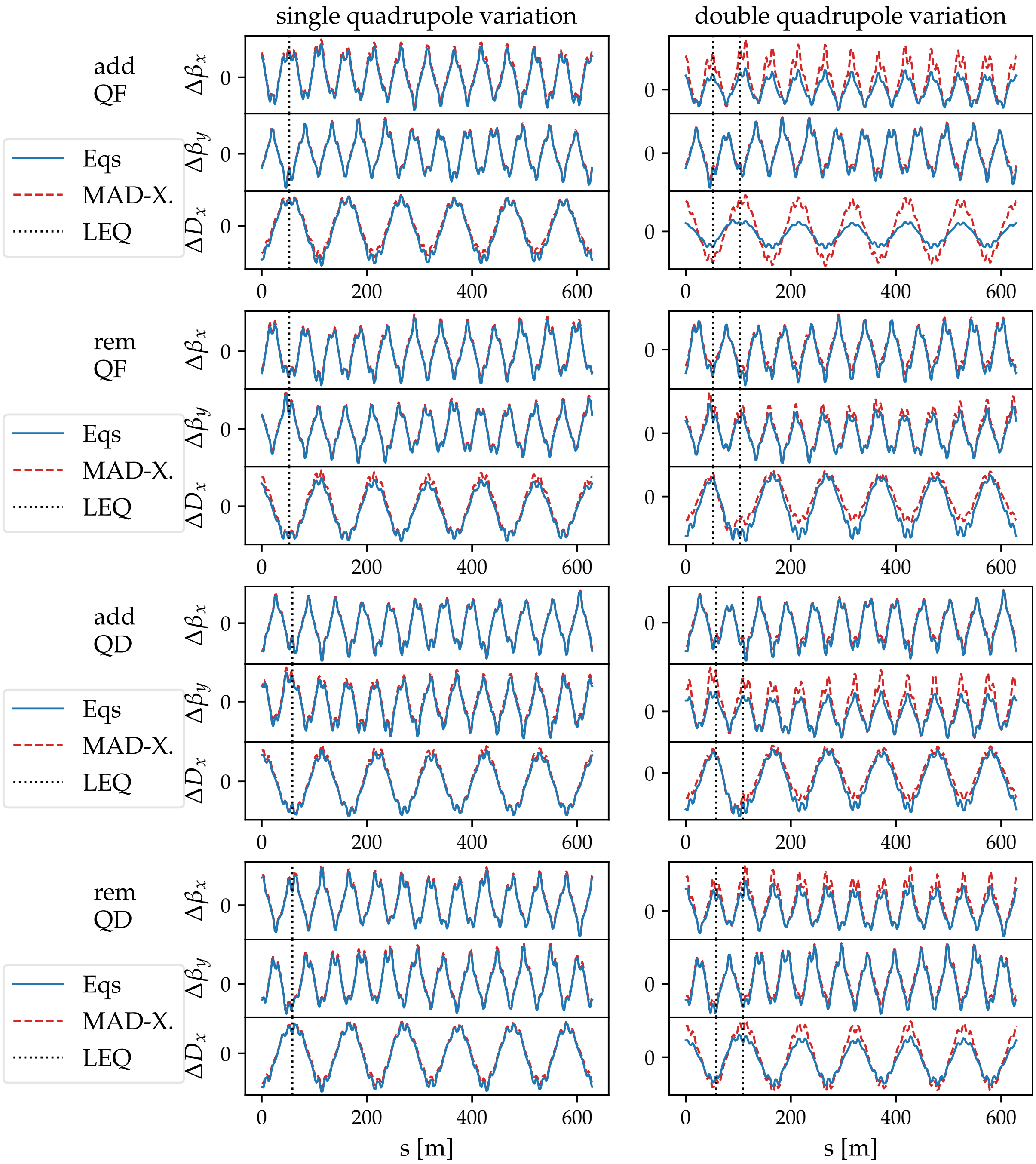

FIGURE 4.12: Tests of expanding the linear imperfections equation to predict the outcome of adding or removing a quadrupole to the PS lattice. QF stands for focusing quadrupole and QD for defocusing quadrupole. The dotted line represents the locations of the excitated LEQs.

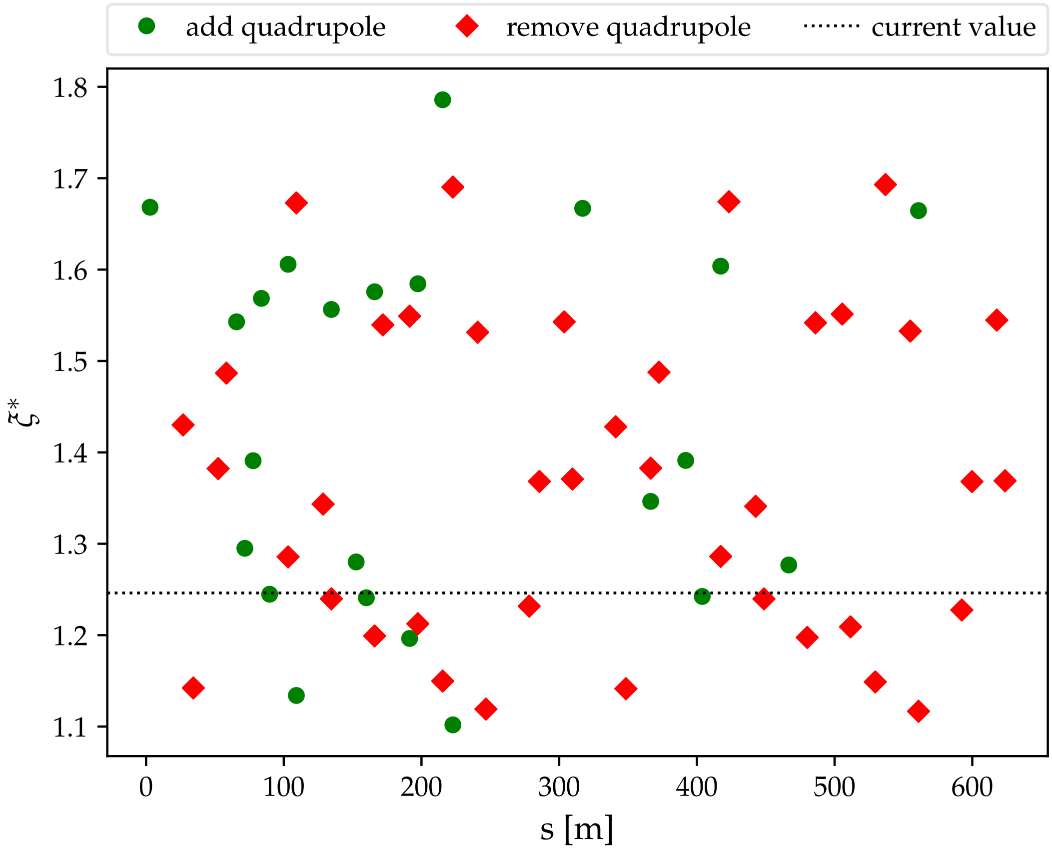

FIGURE 4.13: ξ^* for any possible addition or removal of a single quadrupole to the current lattice. Green dots are at the locations where a single quadrupole can be added and red dots represents a removal of a quadrupole at that location. The black line represents the current ξ^* value.

	remove LEQ in SS	add LEQ in SS	ξ^*
0 changes			1.2460
1 change	90		1.1141
2 changes	56	86	1.1707
3 changes	10, 90	26	1.1097
4 changes	10, 90	26, 36	1.1094
5 changes	21, 22, 90	13, 14	1.0908

TABLE 4.1: Changes to the current lattice to get the best quadrupole configurations based on the branching study.

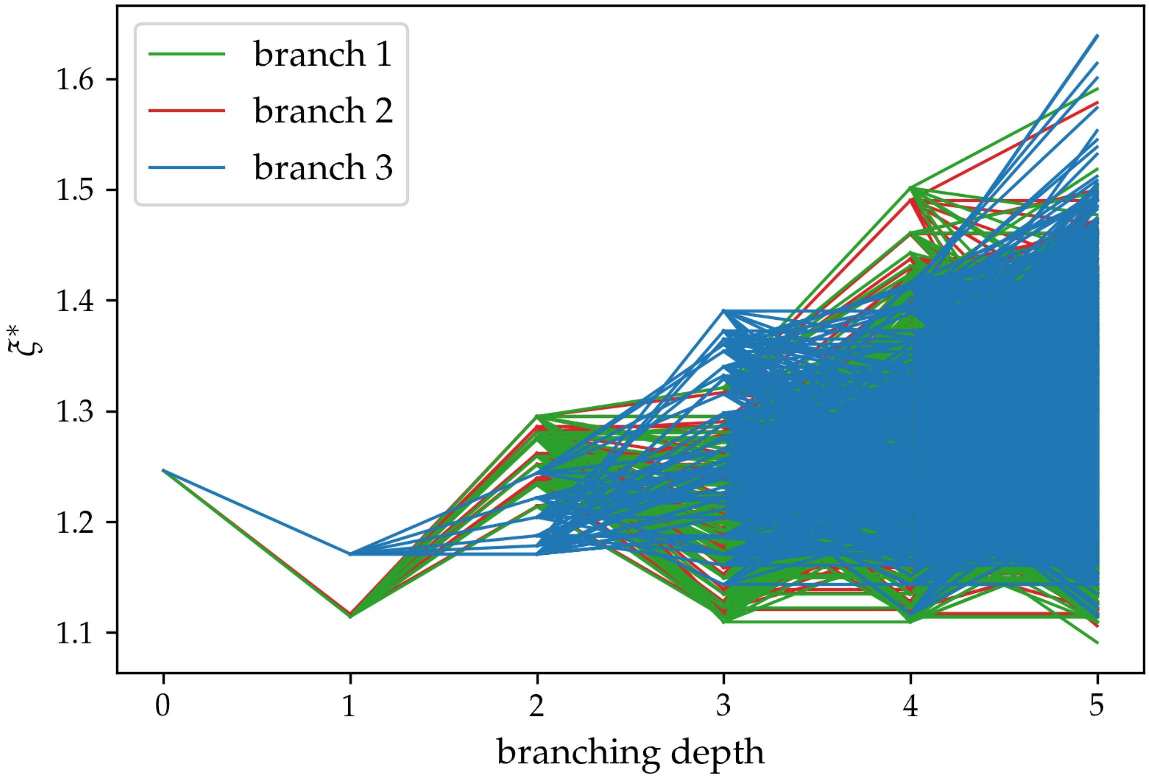

FIGURE 4.14: Iterative prediction of ζ^* in function of the changes to the original configuration to form a branching structure. Only 3 branches are shown for better visibility. The branching depth equals the number of changes.

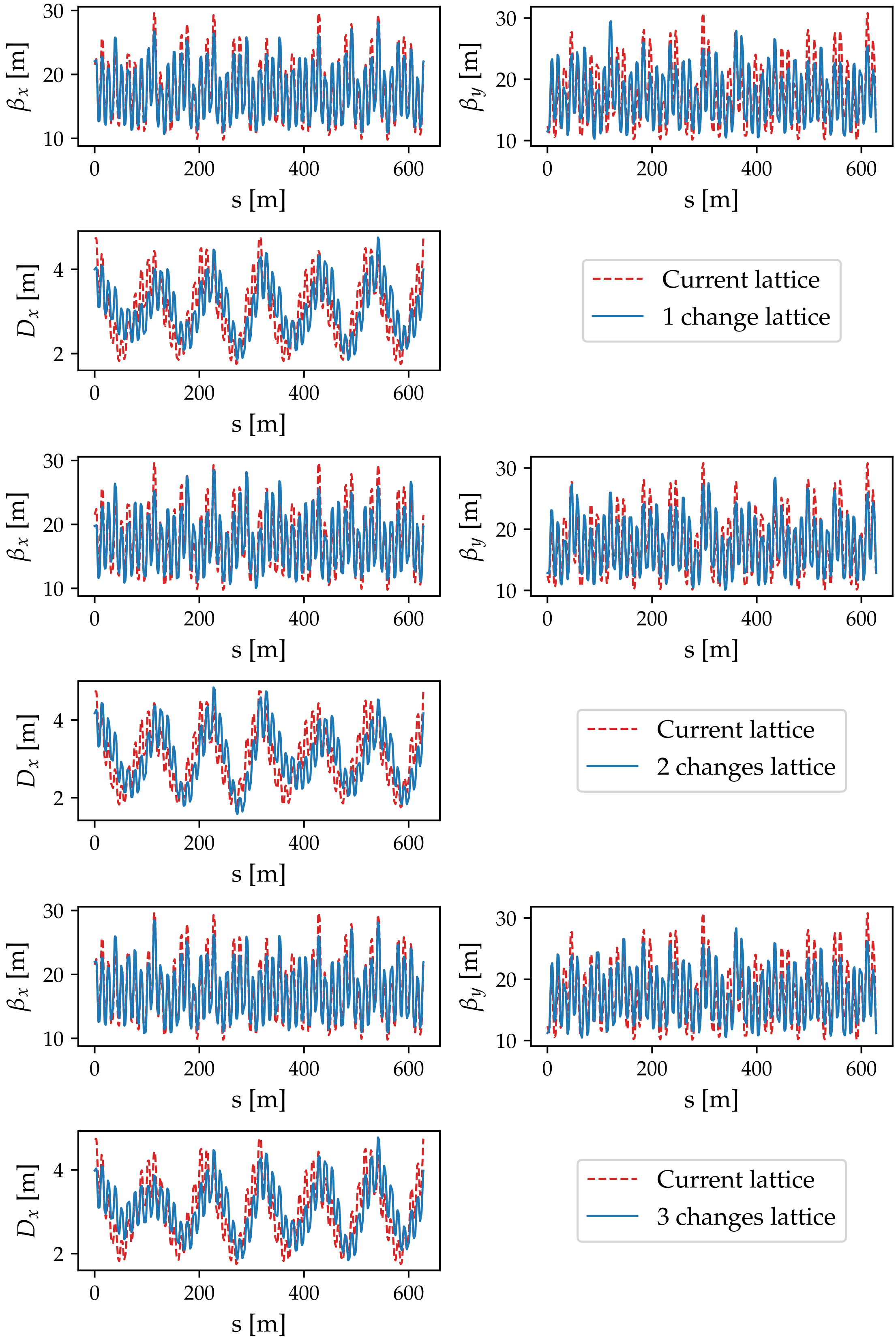

FIGURE 4.15: The resulting optics for the best configurations from the branching study 4.14. The modified quadrupoles are listed in Table 4.1.

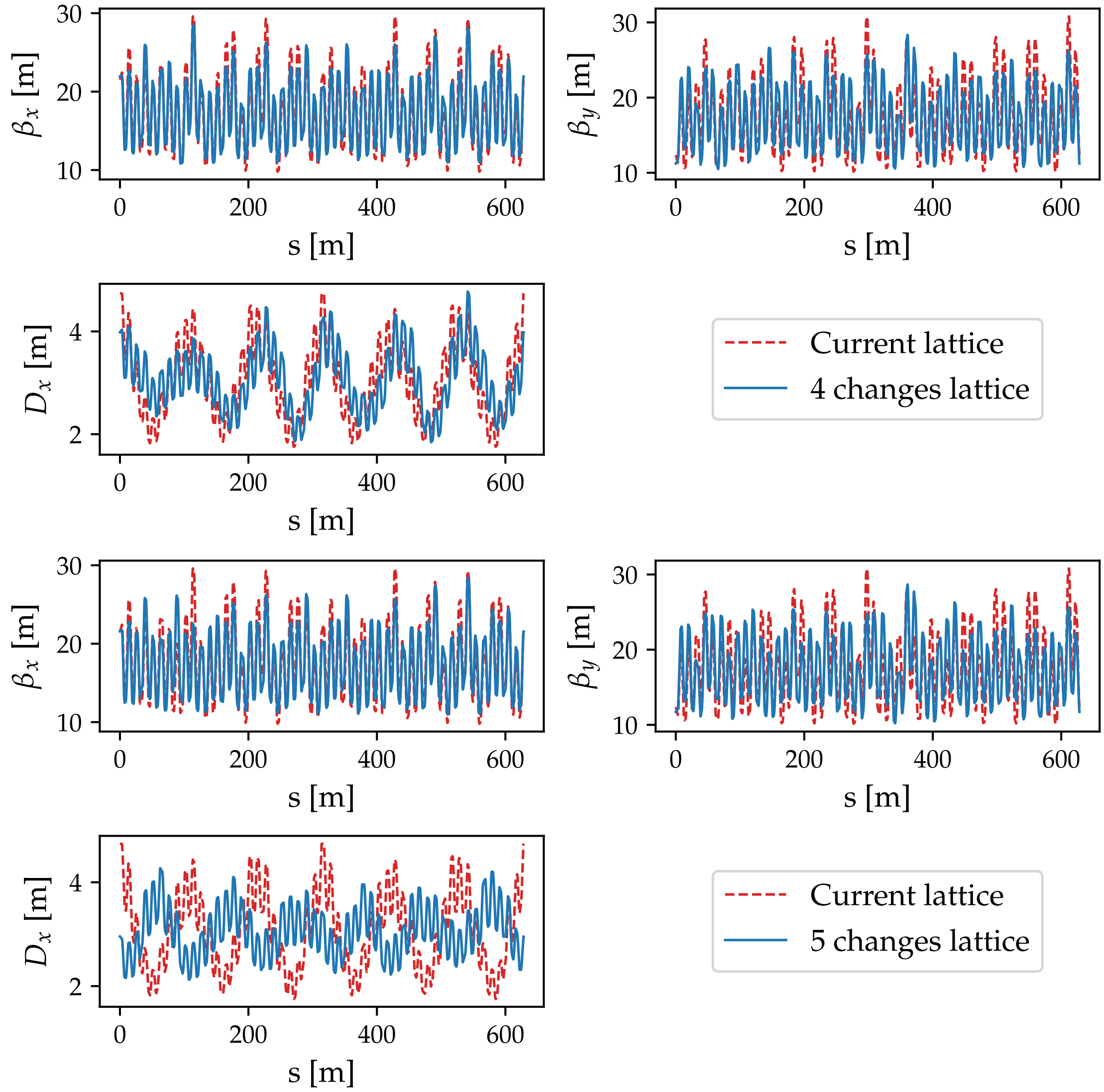

FIGURE 4.16: The resulting optics for the best configurations from the branching study 4.14. The modified quadrupoles are listed in Table 4.1.

4.3 Emittance blow-up investigation with space-charge forces

The optimal LEQ configuration as well as the configurations with less changes need to be tested using space-charge simulations. While single-particle calculations do not change over the number of turns, space-charge effects are noticeable on a scale of many turns. The space-charge simulation framework uses the same initial beam distribution for every working point in the transverse tune scans, causing a mismatch between the initial parameters and the stable equilibrium. This is intended, as it corresponds to the operational setup where the transfer line is usually not rematched after a modification of the working point in the PS. The emittance has to be measured after filamentation of the distribution once the beam reaches a stable equilibrium. Contrary to the MAD-X simulations, the space-charge framework only allows to save the beam optics at one specific location every turn, making it impossible to compare the βs and dispersion functions over the whole lattice as it was done in the previous section. While the transverse distribution is calculated for the nominal working point at the start of the simulation for every test lattice, the initial longitudinal beam distribution is calculated for the current lattice and is not recalculated for the different quadrupole configurations leading to an additional small beam mismatch.

The emittance until 2200 turns ($\approx$ 5 ms after injection) is simulated and saved for every working point to perform a horizontal and vertical tune scan, shown in Fig. 4.17. The emittance presented on the figure is the emittance at turn 2200. The results show many interesting things, although the beam blow-up is still present for both planes. Most notably is the reduction of the vertical emittance blow-up, around 58 % at $Q_x = 6.10$, for every configuration except for the 4 changes lattice compared to the current lattice. The horizontal blow-up also shows some improvement for some tune values, from 10 to 35 % at $Q_y = 6.10$. The 3 changes lattice shows the best vertical blow-up reductions of 65 % close to the integer tune compared to the other lattices, while the horizontal emittance of this lattice shows the least amount of improvement for most of the scan. The opposite can be said about the 4 changes lattice, where the vertical emittance shows no improvement and the horizontal blow-up does show improvement ($\approx$ 33 %). At the moment both β-functions have equal contributions to ξ, but by appropriate weighing further improvement in one plane might be found at the cost of the other plane. Additionally, the correlation between ξ and emittance blow-up can be studied to find other suitable objective functions. The study was performed close to the integer resonance at $Q_z = 6.0$ to enhance the optics beating and emittance blow-up. In practice, these working point are not used so Fig. 4.18 shows the results of the space-charge study in the region closer to the machine working point for high-brightness beams. The 1 change, 5 changes, and optimised lattices show improvement in both planes. The horizontal blow-up is, respectively reduced by 30 %, 40 % and 45 % at $Q_y = 6.16$ and the vertical blow-up by 60 %, 58 % and 82 % at $Q_x = 6.19$. The 1 change lattice is especially promising since this can be tested directly in an experimental setup.

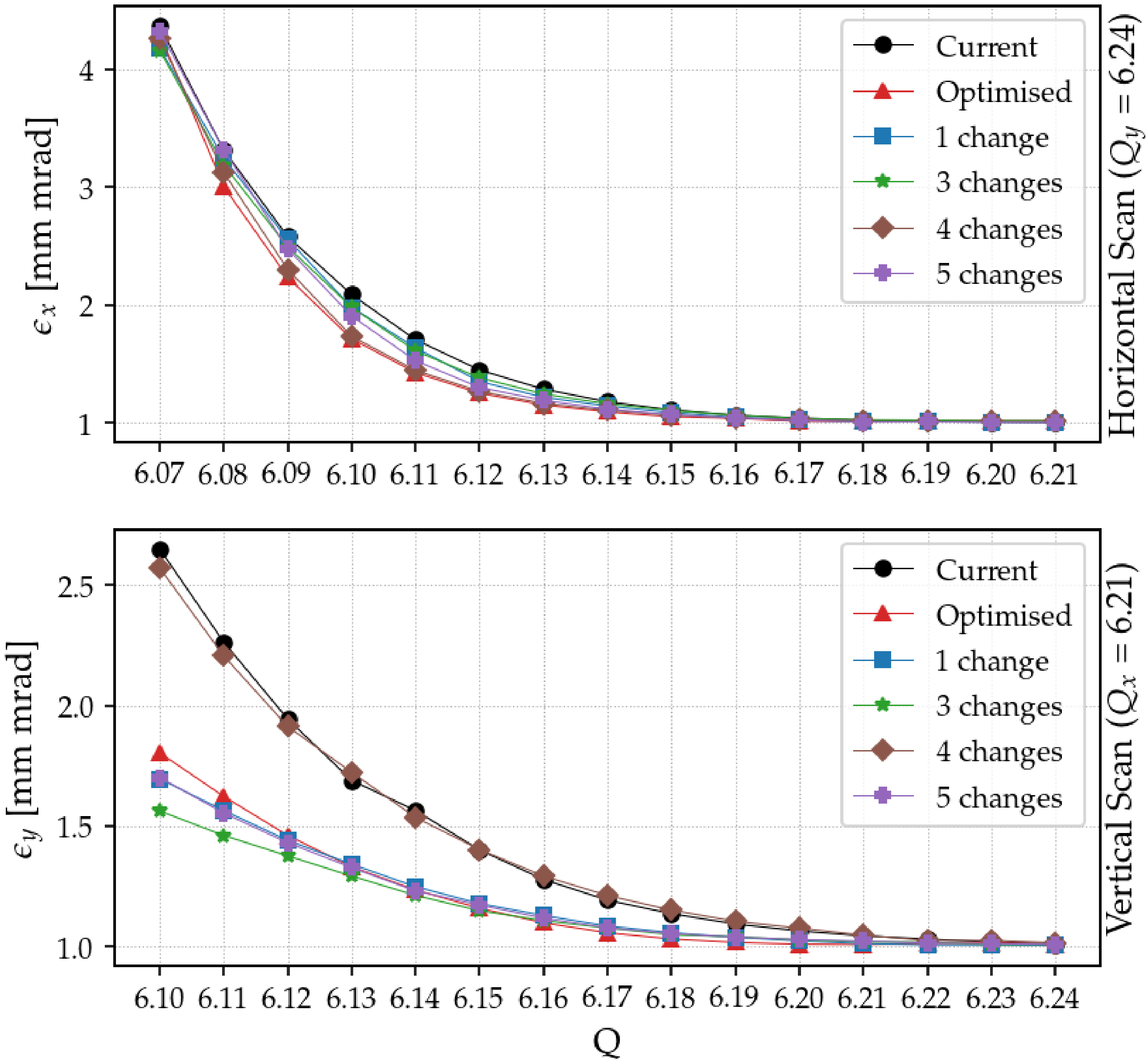

FIGURE 4.17: Evolution of the normalised emittance 5 ms after injection obtained with space-charge simulations using different quadrupole configurations. The horizontal scan is performed at the WS 65, the vertical scan at the WS 64.

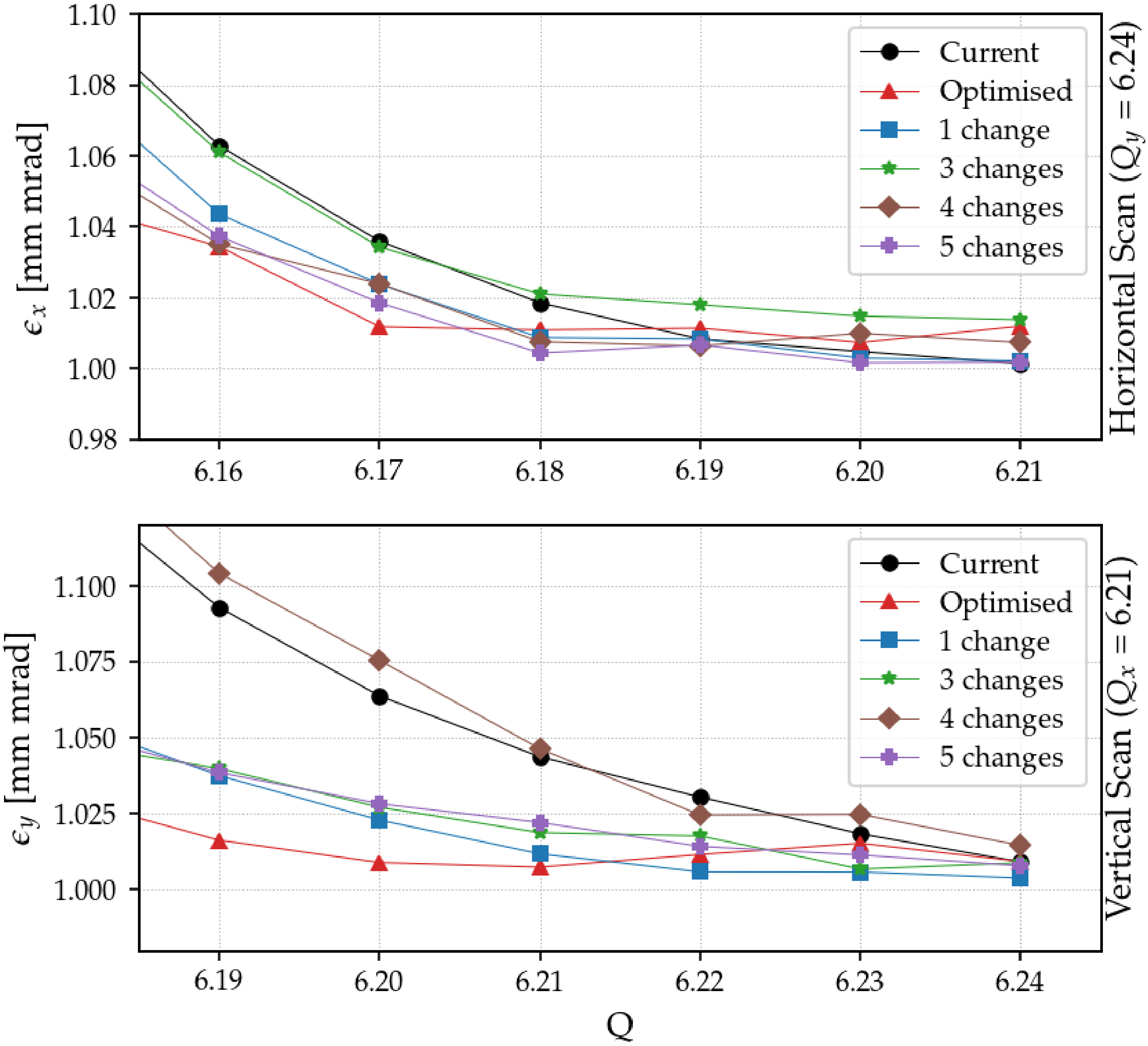

FIGURE 4.18: Zoomed-in version of Fig. 4.17 to increase visibility around the working point range of high-brightness beams.

4.4 Conclusion

In the last 5 decades, the PS went from the ideal 50 LEQ lattice to the current 40 LEQ lattice. The irregular placements of the LEQs for the current lattice leads to large optics beatings and therefore to an emittance blow-up near integer working points. In this chapter the re-positioning of the LEQs was investigated to reduce the optics beatings, and therefore the emittance blow-up. A reduction of the beatings was realised through an optimisation algorithm or by iteratively either removing or adding an LEQ to the current lattice. To compare the quadrupole configurations with each other, an objective function ξ^* was defined that quantifies the optics beatings based on the standard deviations of the β- and dispersion functions around the machine. As a result, 5 interesting quadrupole configurations were identified, which each lead to greatly reduced ξ^*. Additionally, these configurations were simulated with the inclusion of space-charge forces to examine the reduction of emittance blow-up. For all cases, a significant reduction of emittance blow-up in at least one of the transverse planes is observed. The most notable quadrupole configuration found by the studies is the lattice where only LEQ 90 is removed, as it showed a blow-up reduction of 10 % in the horizontal plane at $Q_y = 6.10$ and a reduction of 58 % in the vertical plane at $Q_x = 6.10$. This configuration is easily testable in an experimental setup since it only requires to keep LEQ 90 at zero strength. The variation of how each lattice reduces the emittance blow-up gives insight to a possible redefinition of ξ, by giving more emphasis on one plane over the other. Since the vertical tune spread for LHC-type beams is larger than the vertical tune spread, reducing the blow-up in the vertical plane is more important. The objective function can also be improved upon, by studying its correlation with the emittance blow-up through space-charge simulations. This would aim at identifying a quadrupole configuration for which the emittance blow-up is reduced in both planes.

5 Zero-Dispersion Optics to Improve Horizontal Emittance Measurements

In several research accelerators that were built in recent times there is a special section where the dispersion is brought to zero, called a dispersion suppressor. This special section is used to infer information about the beam distributions in the transverse planes using the WS or similar instrumentation. Eliminating the dispersion $D_z(s)$ at the WS proves useful since the true aim of beam size measurements is to infer ϵ_z through Eq. 2.6 assuming the β_z function is also known. Because of the very regular lattice, the PS has no such section so the beam size contains both betatronic and dispersive contributions. The design vertical dispersion is zero throughout the whole ring since there is no beam-guiding in the vertical direction.

For high-brightness beams that are needed for the LHC, there is a large horizontal emittance blow-up ($\approx 40\%$) measured between the PS Booster (PSB) and the PS itself, as shown in Fig. 5.1. In the framework of the LIU project, this emittance blow-up has been extensively investigated over the last years [41–43]. There are many contributors to the beam blow-up and to properly study all the sources, high-resolution beam size measurements are required. An optics configuration with zero horizontal dispersion at the location of a horizontal WS would deconvolve the horizontal (betatronic) and longitudinal (dispersive) distributions, and hence remove a known source of uncertainties. The zero-dispersion optics must be reachable fast after injection, where the emittance blow-up occurs, and must not differ too much from the nominal optics because the tune spread of the LHC beams is large [44]. Another aspect to be considered is that a large optics perturbation leads to a shift of the nominal working point. Due to the large tune spread particles might overlap with excited betatronic resonances that the beam did not experience with nominal optics.

A previous study showed successfully that lowering the dispersion in the PS to zero, at locations where the beam size is measured, is possible [45]. The study achieved this by individually varying ten adjacent LEQs (see Fig. 5.2). The study concluded that reaching zero dispersion is possible, but the quadrupole strength limit is reached and the other optics functions are also distorted. The study was able to reach zero dispersion optics by varying many different sets of adjacent quadrupoles, these are called active sets for the continuation of this chapter. Each different active set distorted the optics in a unique way. Therefore, one can assume that there is an active set of not necessarily adjacent quadrupoles that forces the dispersion to zero while minimally affecting the other optics functions.

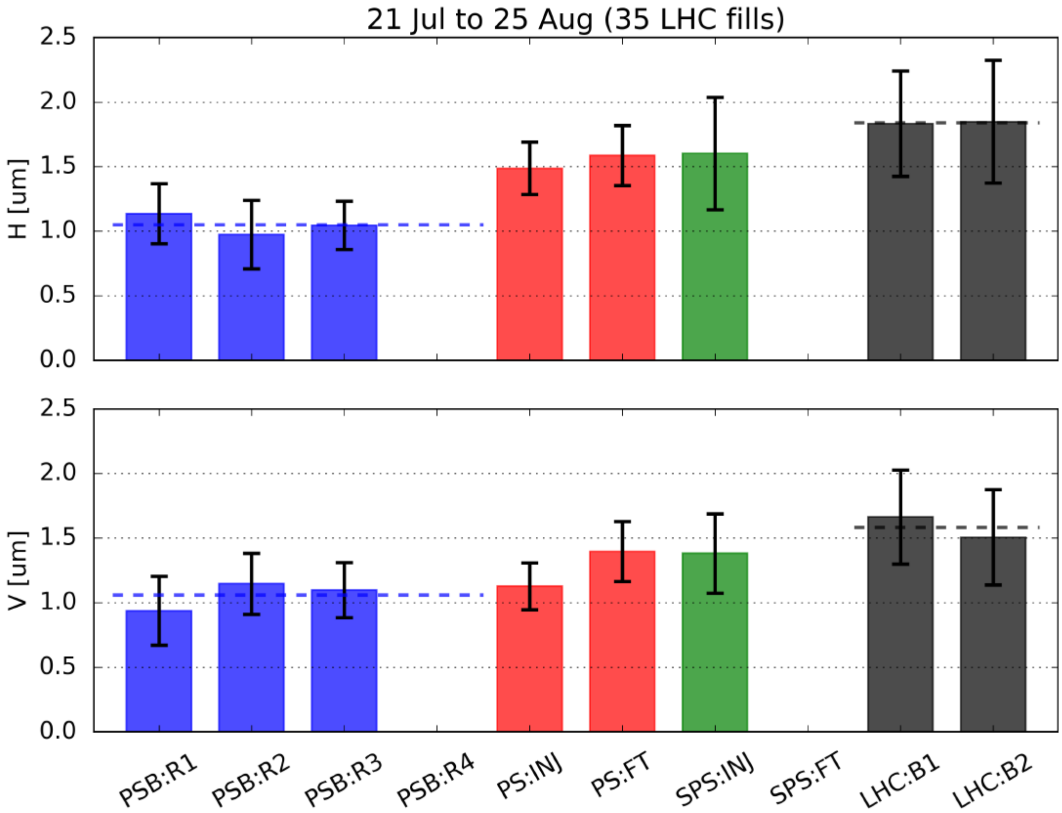

FIGURE 5.1: Details on the emittance evolution along the LHC injector chain. A horizontal emittance blow-up has been regularly observed between PSB extraction and PS injection for high-brightness LHC beams. Figure from [40].

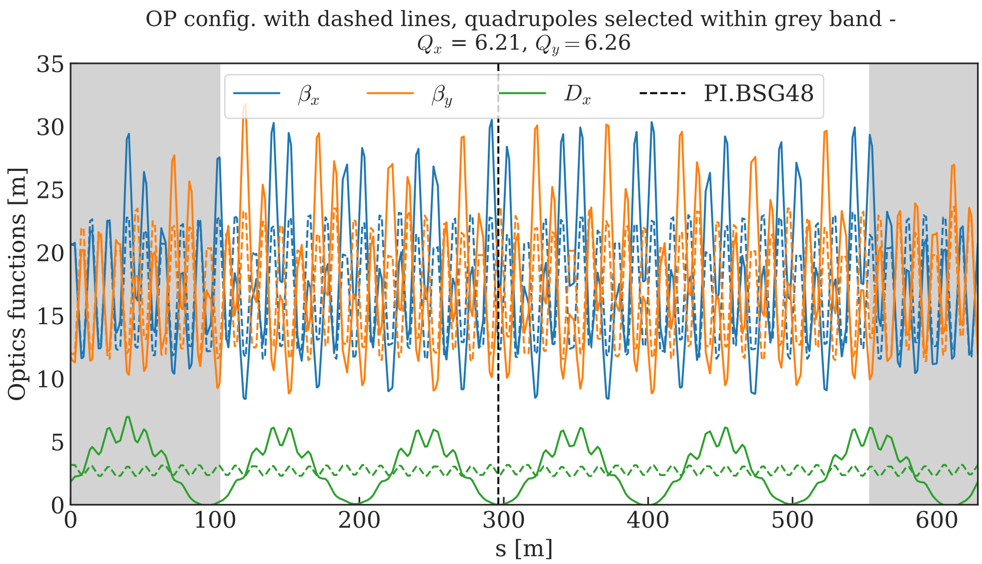

FIGURE 5.2: Optics functions when reducing the dispersion at PI.BSG48 to zero with 10 adjacent quadrupoles within the grey band. The distortion compared to the nominal optics (see Fig. 3.3) is clearly visible. Plot from [45].

After the current shutdown the PS will be equipped to preserve the transverse emittances of higher-brightness beams in the LIU era. Therefore, and due to the fact that the beam blow-up occurs at injection, the lattice used to study a new zero-dispersion optics configuration in MAD-X simulations must replicate the new PS lattice at injection energies of 2 GeV. Note that moving from 1.4 to 2 GeV over the shutdown limits the LEQ strengths more because of the higher beam rigidity.

5.1 Single-particle study

In this chapter the zero-dispersion optics study is continued by shifting the focus from only reaching zero-dispersion to reaching zero-dispersion while minimising the variations of the β-functions and keeping the working point constant. Thus, techniques discussed in Chapter 4 are implemented. Utilising numerical optimisation techniques and the linear imperfection equations, active LEQ sets are pursued that satisfy all the conditions for a single beam measurement location.

To begin abstracting the zero-dispersion optics study into a numerical optimisation problem, the quadrupole strengths are the clear choice as optimisation variables. Secondly, the bounds of the problem must force all possible solutions to reach zero dispersion at the specified location. This is accomplished by setting the quadrupole strength limits as bounds and introducing the extra bound that superimposes the contributions of the individual quadrupoles on the dispersion at one location. This bound is of the form

$$D^* = D_0 + \Delta D_{k_1} \times \delta k_1 + \Delta D_{k_2} \times \delta k_2 + \ldots + \Delta D_{k_n} \times \delta k_n, \tag{5.1}$$

where D_0 is the initial dispersion, D^* is the dispersion after varying the quadrupoles and ΔD_{k_i} are the scalars proportional to the effect of a quadrupole variation of size δk_i on the dispersion at that location. Here the dispersion-beating is assumed to be directly proportional to the quadrupole variation. This is not a known property and is therefore investigated in the scope of the work carried out in this chapter. The results that show this is a valid assumption are presented in Fig. 5.3. The dispersion-beating equation is used instead of the results from MAD-X to reduce computing time in the optimisation algorithm.

The objective function of the optimisation algorithm must then minimize the change in optics. From Eqs. 2.30 and 2.8, one can notice that the tune-shift and β-beating caused by varying one quadrupole is directly proportional to the quadrupole strength error. Therefore, if the quadrupole variation is small, the resulting optics distortion is also small. The goal of the optimisation algorithm developed for the study is consequently to keep the quadrupole variations δk_i minimal, since every possible solution will lead to zero horizontal dispersion at the desired location due to the bounds. This leads to the objective function

$$\text{minimize } \delta k_1^2 + \delta k_2^2 + \ldots + \delta k_n^2,$$

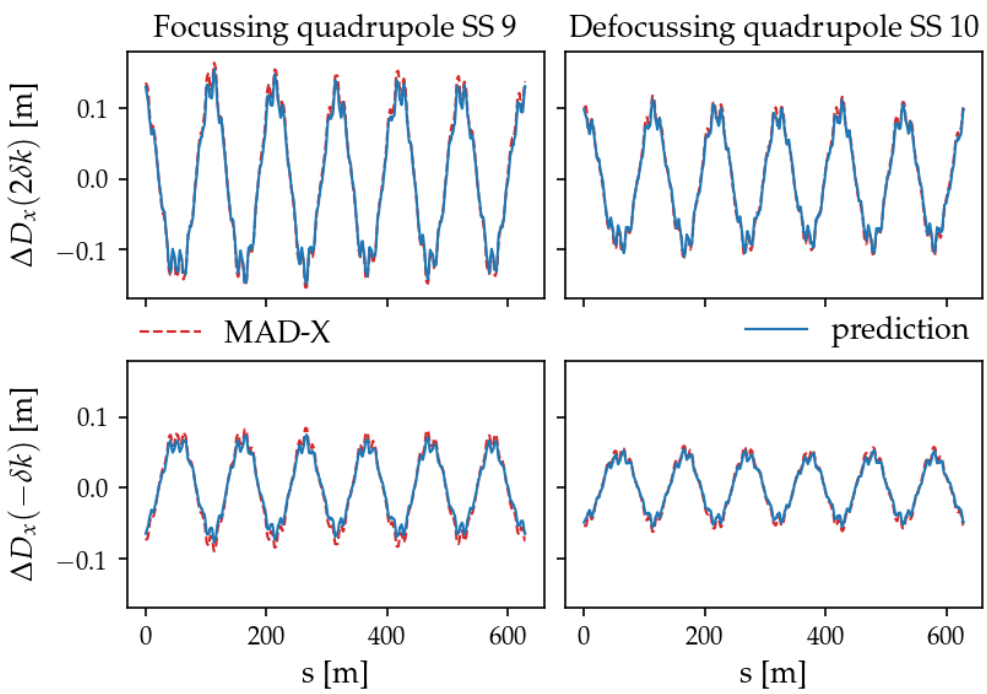

FIGURE 5.3: Tests showing the response of the dispersion function to a single quadrupole error in order to investigate proportionality. The predictions in blue are obtained from Eq. 2.8 with $\delta k = 0.001$ and then multiplied with a factor to mimic the Δk used in MAD-X simulations.

where the squares of δk_i are used instead of the absolute values to attain a convex quadratic optimisation problem which is very common and more studied, hence the publicly available solvers are usable. Additionally, this optimisation problem is well defined in contrast to the one in Chapter 4 and therefore an investigation comparing multiple solvers is trivial. The public library Python Software For Convex Optimization (CVXOPT) was used as solver [46].

Initially, all 40 LEQs are used in the optimisation. However, to see if the same result can be achieved by less active quadrupoles, the active number of LEQs is iteratively reduced by one LEQ until the quadrupole strength limit is reached. The reduction is realised with the following reasoning: If $|\delta k_i|$ is large for a certain quadrupole, that quadrupole heavily forces the dispersion to zero. Hence, the LEQ with the lowest $|\delta k_i|$ has the least influence in this problem and can be removed from the equations. With the implementation of this last ingredient, the full zero-dispersion simulation framework is built. A zero-dispersion simulation starts with the active set that consists of the current LEQ lattice. The quadrupole strengths of the active set, starting from their nominal settings, is then optimized by the numerical optimisation algorithm. The lowest $|\delta k_i|$ is taken from the results and the corresponding LEQ is removed from the active number of LEQs. This process is repeated, starting from the nominal optics in every step, until the optimisation algorithm no longer finds a solution. At this point it is no longer possible to obtain a zero-dispersion optics, while staying within the LEQ strength limits.

Figure 5.4 shows the progress of this method for one WS location. The β-functions and tunes display minimal optics distortion compared to the nominal optics when using 15 LEQs and above. When few quadrupoles are used, the variations in quadrupole strengths become too large for the linear imperfection formulae to hold true, similar to what was presented in Fig. 4.12, leading to non-zero dispersion optics at the WS. In these cases, it is speculated that the set of active quadrupoles are optimized but their strengths are not. Hence, zero-dispersion optics can still be achieved by repeating the optimisation using the first results as initial optics. While there is no real limit to the amount of LEQs that can be used for this objective, a low number of LEQs is preferred. This simplifies an experimental test of the identified configuration.

This method is applied to multiple beam measurement locations discussed in Chapter 3, such as WSs, SEM grids and BGIs. To avoid cases where the linear approximations stop being valid, the iterative reduction of the active set is halted at 15 LEQs. The dispersion function, other optics distortions and the tune-shifts for 15 quadrupoles using the optimisation algorithm are shown in Fig. 5.5 and the corresponding quadrupole strengths are presented in Table A.2. These results are the optimum solutions found due to the minimum number of quads and minimal perturbation of all optics, while still reaching zero dispersion at the beam measurement location.

5.2 Investigation of the impact of direct space charge forces

In the previous section, the dispersion function is successfully forced to zero for single-particle calculations where space charge is neglected. Here, space charge forces are included to examine whether the dispersion behaves differently and whether space charge needs to be included in the optimisation algorithm. This is done by using the space charge framework discussed in Chapter 2 and the results obtained in the previous section.

In practice, the dispersion only needs to reach zero during the beam profile measurements with the WS. Before and after the measurements the beam must be in its nominal state. This can be accomplished by using the LEQs and varying their electric current input individually using a knob that continuously ramps their strength up or down. This knob is a function in the control system, which tells the system what to do dependent on the knob's value. In the case of this study, the knob zero value would be the nominal optics and one would stand for the zero dispersion optics.

Using the space charge framework active LEQs can be ramped up in a similar way as they would inside the PS. This is achieved through varying the strengths discretely every turn. There is a small time period at zero dispersion provided for the beam profile measurement, using the quadrupole strengths as shown on Fig. 5.6.

The optics of the single-particle calculations from MAD-X are simulated as the periodic solution to a defined magnetic sequence. This contrasts the space

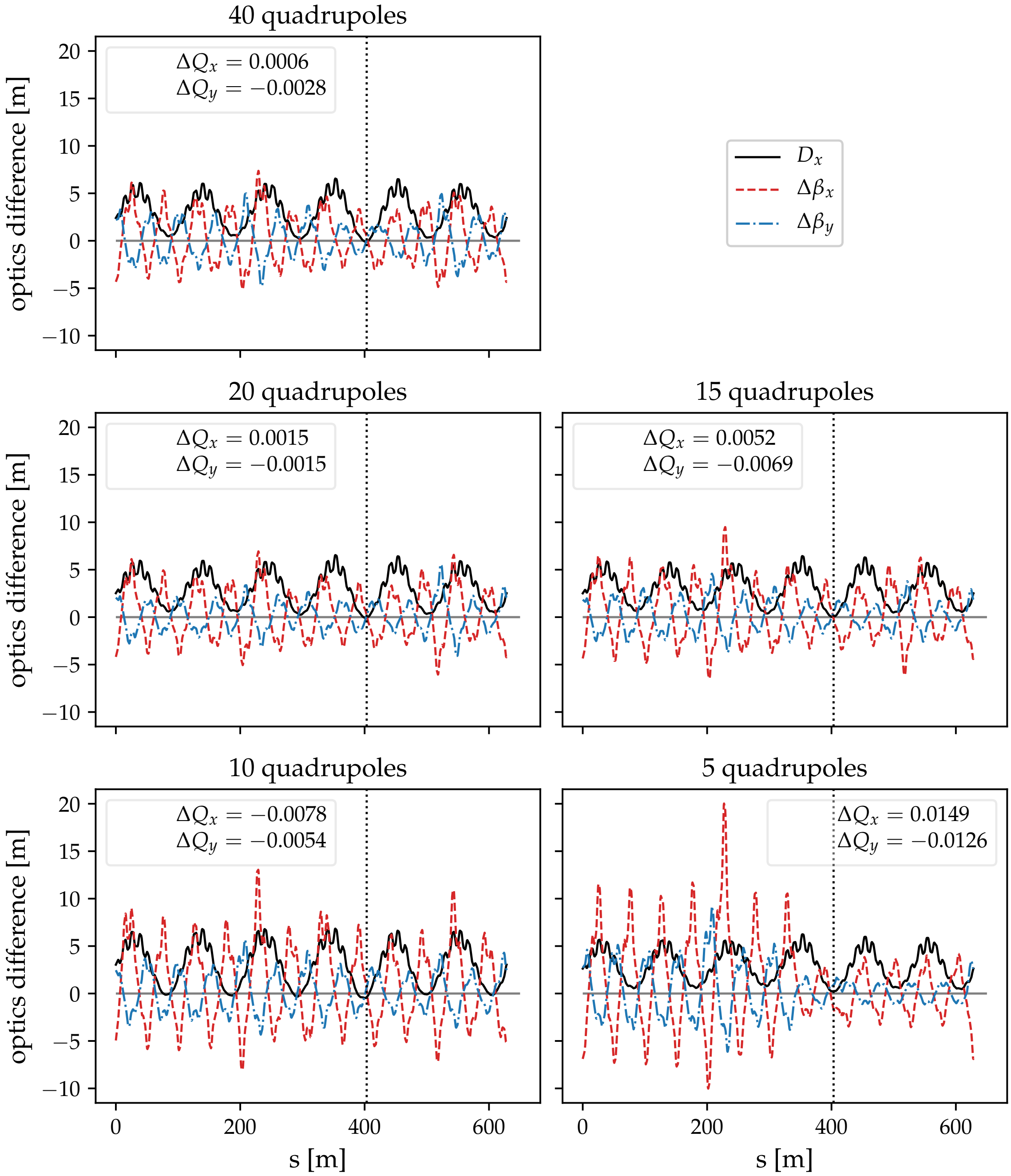

FIGURE 5.4: Iterative optimisation from 40 LEQs to 5 LEQs to set the dispersion at WS 65 to zero. The perturbation of the β-functions compared to the nominal optics as well as the tune-shifts are also shown. The black dotted line represents the location of the WS.

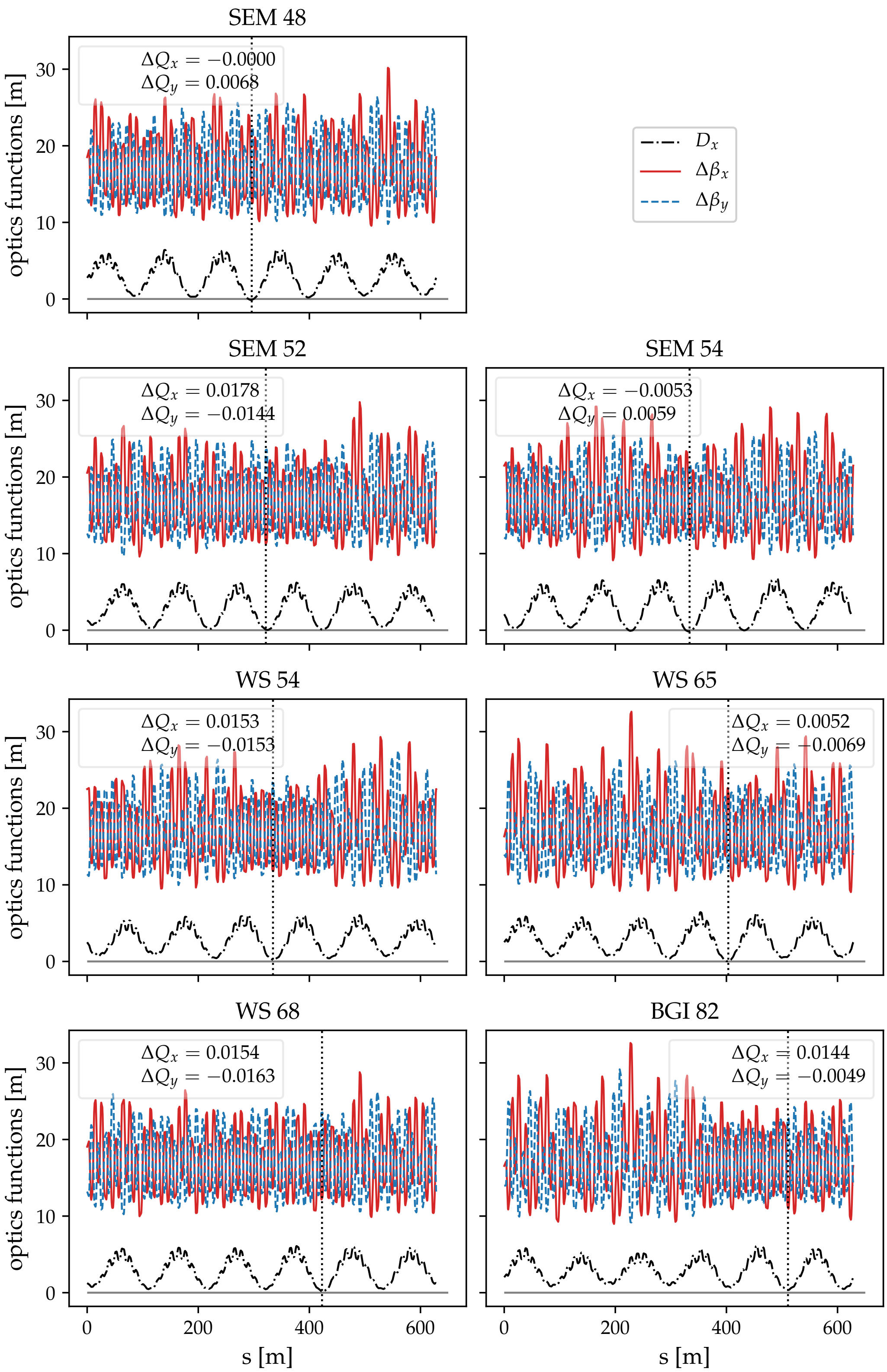

FIGURE 5.5: Zero-dispersion optics configurations obtained at different beam instrumentation when using 15 LEQs. The quadrupole locations and strengths were obtained with the optimisation algorithm.

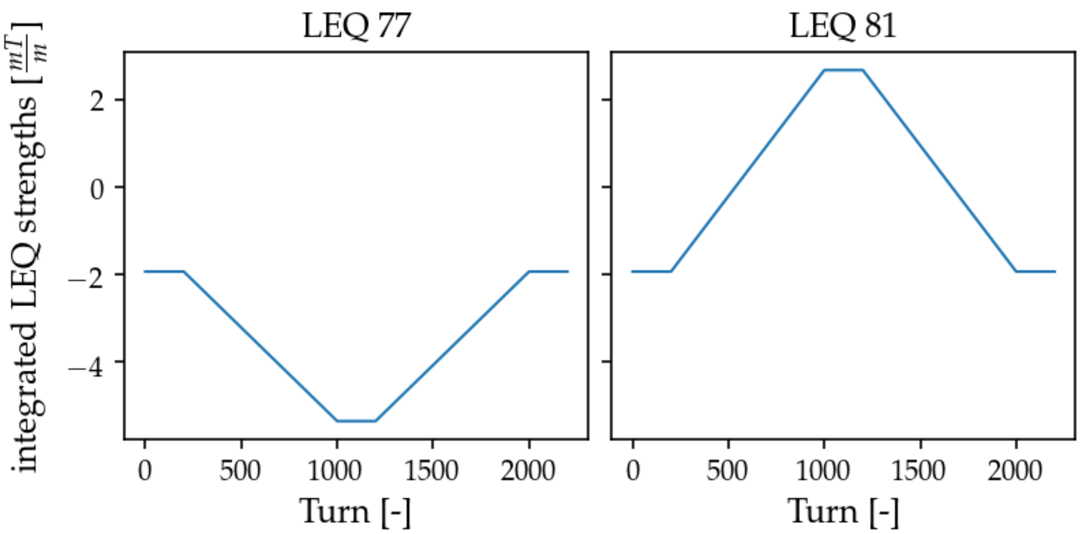

FIGURE 5.6: Ramping of the LEQ 77 and LEQ 81 strengths for moving to zero-dispersion optics at WS 65 using the strengths from Table A.2.

charge framework, where the optics are reconstructed from the distribution of the beam. Because of the different calculation methods, the optics might differ slightly. This is pointed out because the ramping of the LEQs is also simulated without space charge contributions using the same framework for comparison.

As discussed in Chapter 4, the space charge framework only saves the optics at one location in the machine. This location is the starting point of the simulation. The space charge framework was set up to simulate an initial longitudinal distribution at WS 65 and must therefore start the simulation at this point. Thus, only the LEQ strength configuration that forces the dispersion to zero at this WS can be tested. However, one test suffices to understand whether single-particle optimisation is sufficient or space charge needs to be included.

By replicating the beam profile measurement method of the PS, the framework also shows if there are lasting consequences for the emittance after the measurements are done. The results of the dispersion function of the space charge simulations are shown in Fig. 5.7. From the figures, one can conclude that space charge effects cause the dispersion to reach zero more rapidly than without space charge. This means that less quadrupole strength has to be used to reach zero dispersion during operation, which makes it possible to reduce the set of active quadrupoles necessary to maintain stable optics during the beam size measurement. Therefore, the eventual operational knob value will lie between zero and one.

Figure 5.8 presents the horizontal and vertical beam size and emittance during the ramping of the LEQs for a zero-dispersion measurement. The impact on the horizontal emittance is small, which is the plane of interest, but the vertical emittance shows clear growth. In ideal conditions, the horizontal beam size would go through a minimum, whereas the vertical beam size would stay constant. These effects are most likely due to the ramping time being too short for adiabatic ramping. Figure 5.9 shows the beam size progression without space charge effects. The similar variation of the vertical beam size strongly indicates

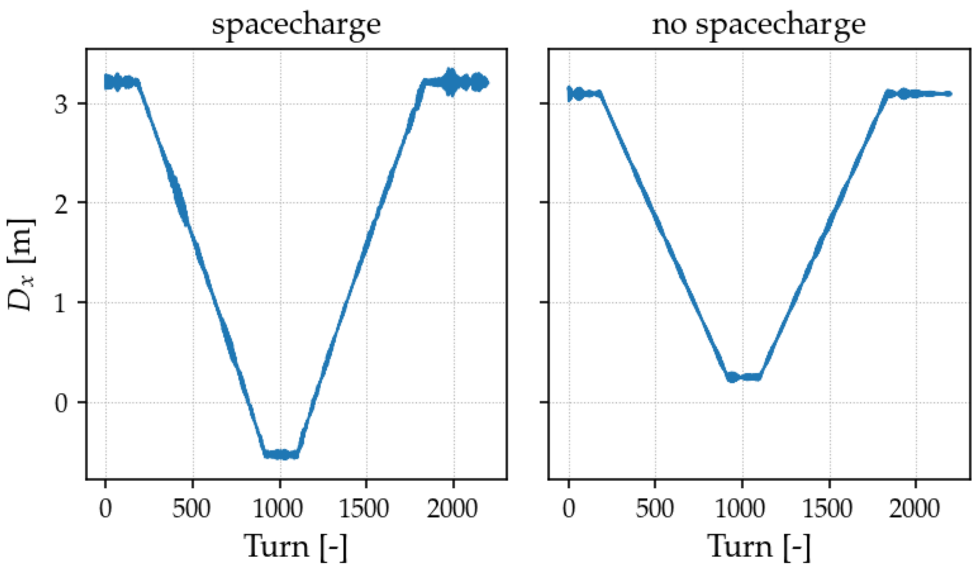

FIGURE 5.7: The dispersion for space charge and non-space charge simulations using the results for the WS at SS 65 from the zero-dispersion study.

that the vertical emittance growth is due to non-adiabatic ramping. However, the difference between initial and final beam size is different for both cases meaning that space charge forces also affect the vertical beam size. Therefore, further investigation of the vertical emittance growth is required.

5.3 Conclusion

The perceived emittance blow-up at injection in the PS is unacceptable for achieving the goals set by the LIU project. The blow-up has many sources which require thorough investigations. Having a good precision on the emittance measurement is essential to achieve this, but emittance measurements have a dispersive contribution due to the absence of dispersion suppressors, which is a known source of uncertainties. The research conducted in this chapter deconvolutes the dispersive contributions from horizontal beam profile measurements around the PS through obtaining zero-dispersion optics with the LEQs, while minimally modifying the nominal optics and keeping the LEQ strengths below their limit. The LEQ strengths needed to achieve zero-dispersion optics are obtained by globally minimising the sum of the squares of the quadrupole strength variations from the nominal optics, while keeping the dispersion at zero at the measurement location and iteratively keeping the least contributing LEQ at its nominal quadrupole strength and removing it from the problem. Zero-dispersion optics are achieved with single particle MAD-X calculations, while the impact of space charge forces leads to a further decrease of the dispersion. Hence, the operationally required quadrupole strengths is smaller than predicted by single-particle simulations and will have less impact on the optics. The emittances are distorted while the optics are moved between the nominal optics and zero-dispersion optics. This shows that the LEQs were

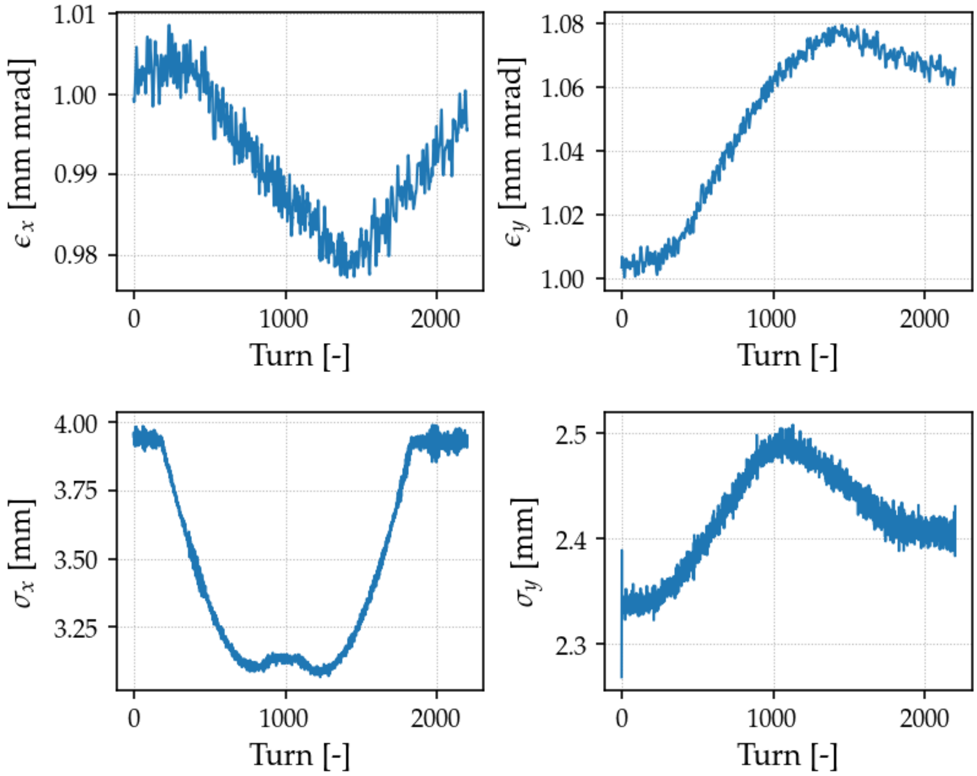

FIGURE 5.8: The horizontal and vertical beam size and emittance evolution during a zero-dispersion space charge simulation.

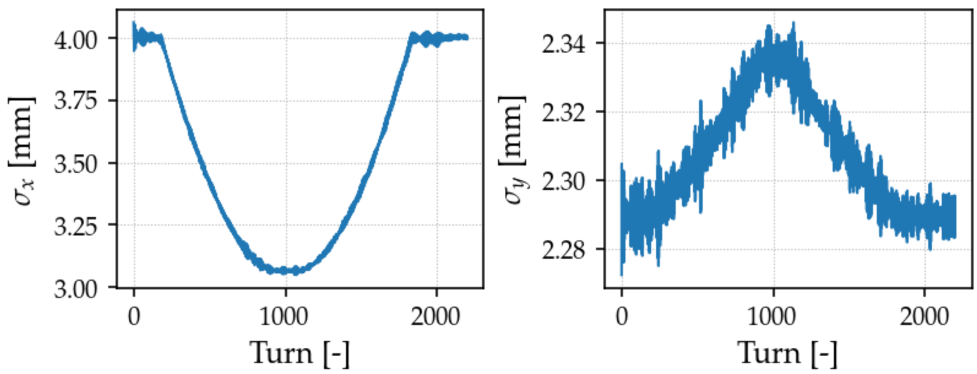

FIGURE 5.9: The horizontal and vertical beam size evolution during a zero-dispersion simulation without space charge.

ramped non-adiabatically in the simulations. The moving of the optics must therefore be further investigated using longer ramping times. The next step is to set up knob functions in an experimental setup using the WS to measure the beam profile for different knob values. At some point, the profile will show minimum beam size and that is when the zero dispersion optics are reached.

6 Quadrupole Gradient Modulation to Improve Transverse Emittance Measurements

The emittance is an important property of a charged particle beam. Having a precise measurement of the emittance allows one to identify and understand sources of emittance growth in synchrotrons and can therefore reduce beam losses especially in transfer lines and at injection. In Chapter 4 a new optics scheme was developed to minimize one known source of emittance growth. Chapter 5 proposes a technique to make emittance measurement in the PS more accurate in the horizontal plane.

Here, the aim is to improve the accuracy of emittance measurements by examining the betatronic part of the beam, whereas the last chapter focused on the dispersive part. As stated before, the beam profile is measured using WSs. Then Eq. 2.6 is used to calculate the emittance. However, in general β-functions cannot be measured at that location. They can be measured at a nearby quadrupole using K-modulation or at the Beam Position Monitors (BPM) using various methods. Subsequently, the resulting β will be propagated to the location of the WS based on the optics models.

The K-modulation technique relies on varying the strength of an individual quadrupole and measuring the resulting tune-shift with a tune measurement system. The variation of the quadrupole strength is commonly sinusoidal, as depicted on Fig 6.1. The function of the magnetic field used to inject, accelerate and extract the beam is called a magnetic cycle. For the K-modulation measurement the beam is usually kept on a plateau of constant energy. For this study, the measurement occurs immediately after injection using an LHC-type cycle where the injection plateau has a length of 1200 ms. Afterwards, the beam is accelerated and extracted. Every cycle, one K-modulation measurement can occur. After one cycle the average $\bar{\beta}$ over an LEQ with length L_{quad} can be found by fitting

$$\bar{\beta} = \frac{4\left[\cos(2\pi Q_0) - \cos(2\pi(Q_0 + \delta Q))\right]}{\delta k L_{quad} \sin(2\pi Q_0)}, \tag{6.1}$$

which reshapes Eq. 2.21 to a usable form. The eventual $\bar{\beta}$ has an error due to the uncertainty of the tune measurements. The size of this $\bar{\beta}$ error, once propagated to the WS, impacts the accuracy of the emittance measurement. The full β-measurement procedure is therefore simulated in this chapter. The characteristics of the sinusoidal δk wave and the number of cycles is studied with respect to their impact on the accuracy of a β-value propagated to a WS.

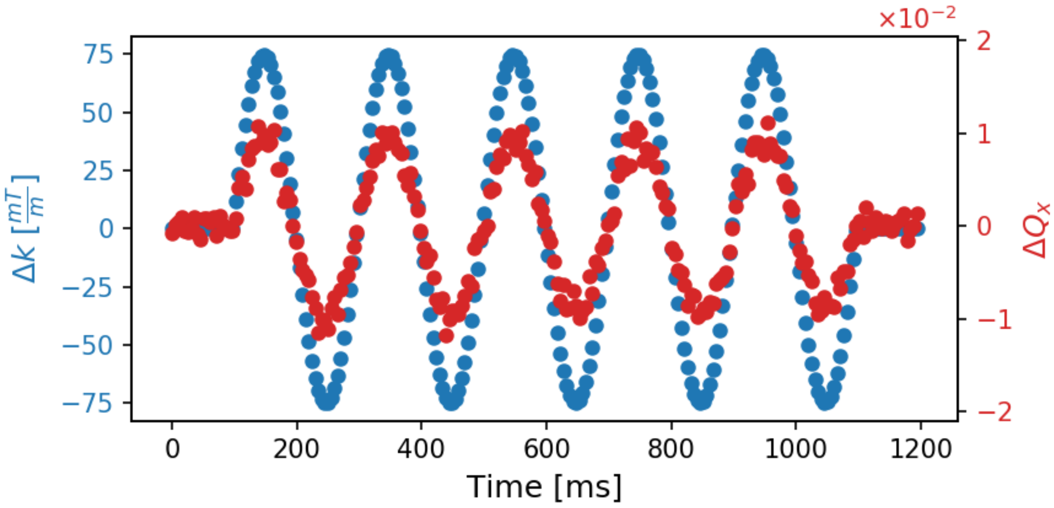

FIGURE 6.1: A sinusoidal δk excitation using LEQ 68 in blue and the resulting tune-shift in red. Δk is the integrated quadrupole strength divergence from its nominal value.

6.1 Impact of the modulation characteristics on the beta-function reconstruction.

For the following simulations the latest PS lattice that is configured for LHC beams was used. The K-modulation measurement has to be performed with a beam with low tune spread to avoid any perturbation. To duplicate the experimental setup, the quadrupole strengths are varied in a cycle of 1200 ms. One sinusoidal measurement is programmed per cycle, which is then used to compute the $\bar{\beta}$ using a fit. Experimentally, this procedure can be repeated on several cycles to improve the precision on $\bar{\beta}$.

Since the LEQs are individually powered, the $\bar{\beta}$s can be evaluated at every LEQ. Experimentally, the tune measurements are inferred from the BBQ system [47]. In this study however the tunes will be directly obtained from MAD-X and an appropriate normal error of $\sigma_Q = 10^{-3}$ is added to replicate the uncertainty of the BBQ measurements. The number of tune measurements that can be recorded within 1200 ms depends on the settings of the BBQ system. For the MAD-X simulations we'll assume that the tune is recorded by the BBQ every 1024 turns which is ≈ 2 ms, but including post-processing time required by the system results in ≈ 5 ms. One $\bar{\beta}$-measurement cycle at LEQ 68 is presented in Fig. 6.1 and the corresponding fitting procedure is shown in Fig. 6.2

The characteristics of the δk excitation of one cycle that could impact the $\bar{\beta}$-measurement are the modulation period and the modulation amplitude. The maximum modulation amplitude is the difference between the LEQ's nominal strength and its strength limit. The modulation period and amplitude are tested in Fig. 6.3, where the amplitude is expressed in percentage of its maximum value. There is a dependency visible on the excitation amplitude, meaning the accuracy of the K-modulation is restricted by the limited strength of the LEQs. Additionally, the full range of the LEQ strengths might not be available

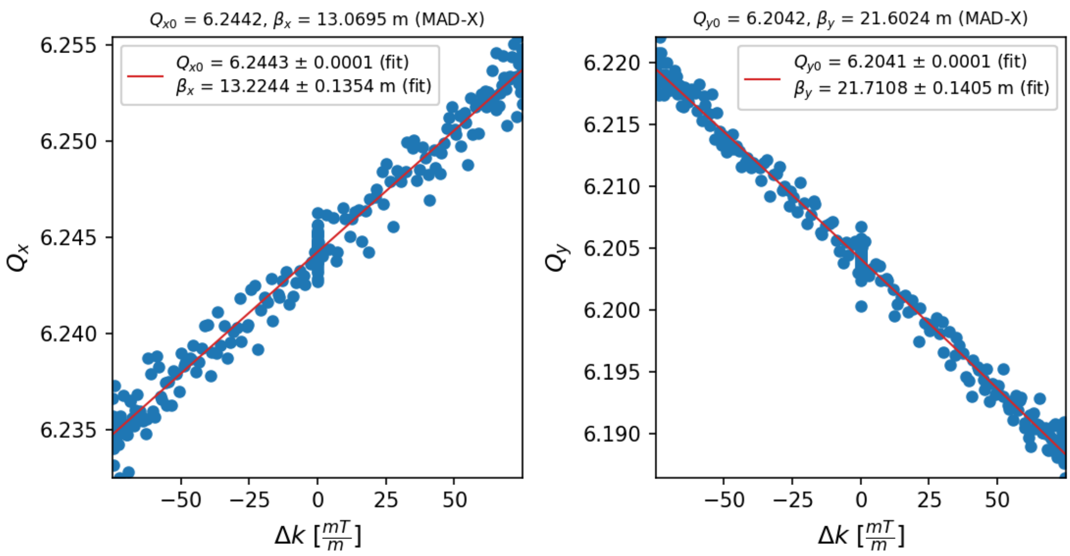

FIGURE 6.2: Fit of a sinusoidal δk modulation and the corresponding tune-shift to Eq. 6.1 to obtain the $\bar{\beta}$ at the excited LEQ 68. The model values obtained through MAD-X are noted on top of the figure.

for some cases since the RMS strength limit might be traversed over a number of cycles causing the LEQ to shut down to protect the power converter. There is no clear reliance on modulation period thus a modulation period of 1000ms is chosen. This makes sure that the beam is varied as slowly as possible.

Apart from the BBQ system uncertainties, there is another error that influences the β measurements. An LEQ is powered through an electrical current. The eventual quadrupole strength of a magnetic element is commonly a function of the applied current, called the transfer function. This function is in general non-linear, because the iron used in the magnet saturates at some point. In the case of the LEQs there is only a single value measured since the LEQs don't have any iron. This single value is labelled the transfer factor in this thesis. The transfer factor between current and quadrupole strength was remeasured in 2003 for an applied current of 6 A [27], the LEQs have a current range of -20 A to 20 A. This measurement was done on a single isolated LEQ. In the machine, the LEQs are surrounded by the iron yoke of the adjacent MUs. This iron yoke could have an impact on the transfer factor. For this reason, the measured transfer factor could be different from the actual factor constituting a systematic error which thus can't be improved upon by multiple measurements. The result of a transfer factor error on LEQ 68 is displayed on Fig. 6.4. Note that here the BBQ system uncertainties were removed from the simulations. The figure shows that a relative error to the transfer factor results in the same relative error to the $\bar{\beta}$-measurement.

Subsequently, the $\bar{\beta}$s have to be propagated to the WS. This is done using the transfer matrix method introduced in Chapter 2. Using this method the particle trajectory can be transferred through magnetic elements. For coherence, the transfer matrix of a horizontally focusing and defocusing quadrupole

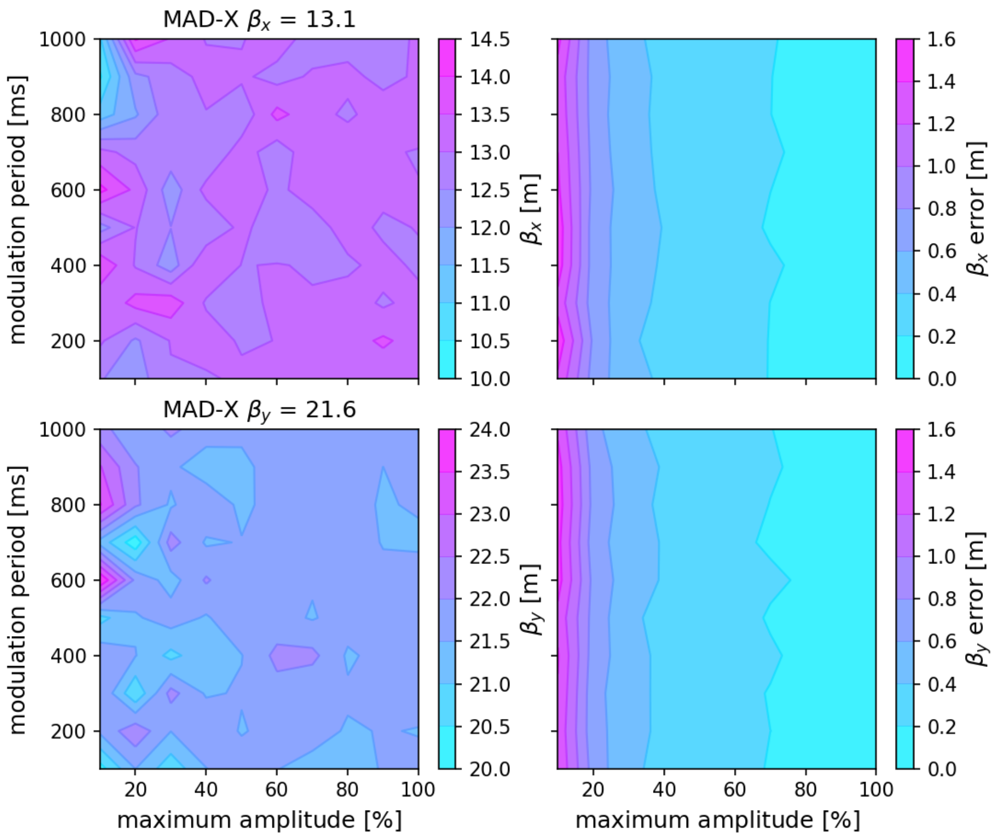

FIGURE 6.3: Dependency of the reconstructed $\bar{\beta}$-function on amplitude and modulation period at LEQ 68. The reconstructed $\bar{\beta}$-values are shown in the left column and the right column presents the uncertainty from the fitting procedure.

are respectively

$$M_{QF} = \begin{pmatrix} \cos\Omega & \frac{1}{\sqrt{|k|}}\sin\Omega \\ -\sqrt{|k|}\sin\Omega & \cos\Omega \end{pmatrix} \quad \text{and} \quad M_{QD} = \begin{pmatrix} \cosh\Omega & \frac{1}{\sqrt{k}}\sinh\Omega \\ \sqrt{k}\sinh\Omega & \cosh\Omega \end{pmatrix}, \tag{6.2}$$

where $\Omega = \sqrt{|k|}L_{\mathrm{drift}}$. From these matrices, the transfer matrix for a drift section of length L_{drift} can be obtained for vanishing gradient k:

$$M_{drift} = \begin{pmatrix} 1 & s \\ 0 & 1 \end{pmatrix} \tag{6.3}$$

Propagation of the β function through magnetic elements is typically explained using properties of the phase space ellipse. The area of the ellipse, defined as the emittance ϵ of an accelerator is invariant throughout the machine. The relation of ϵ to β is

$$\epsilon = \beta x'^2 + 2\alpha x x' + \gamma x^2, \tag{6.4}$$

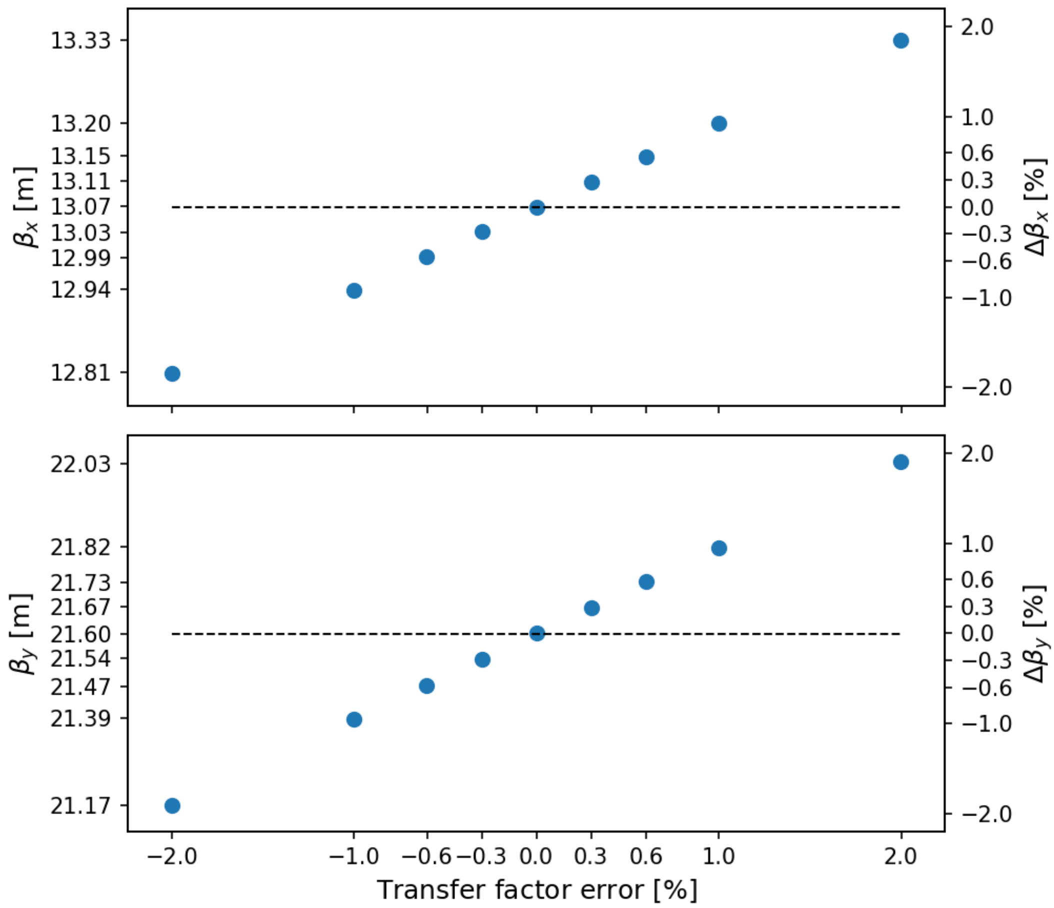

FIGURE 6.4: Impact of the uncertainty of the transfer factor on the reconstruction of the $\bar{\beta}$ function.

with $\alpha = \frac{-\beta'}{2}$ and $\gamma = \frac{1+\alpha^2}{\beta}$. Transferring from $s_0(\beta_0, \alpha_0, \gamma_0)$ to $s(\beta, \alpha, \gamma)$ through an element with transfer matrix

$$M = \begin{pmatrix} m_{11} & m_{12} \\ m_{21} & m_{22} \end{pmatrix} \tag{6.5}$$

leads to the following relation:

$$\begin{pmatrix} \beta \\ \alpha \\ \gamma \end{pmatrix} = \begin{pmatrix} m_{11}^2 & -2m_{11}m_{12} & m_{12}^2 \\ -m_{11}m_{21} & m_{11}m_{22} + m_{12}m_{21} & -m_{22}m_{12} \\ m_{21}^2 & -2m_{22}m_{21} & m_{22}^2 \end{pmatrix} \begin{pmatrix} \beta_0 \\ \alpha_0 \\ \gamma_0 \end{pmatrix} \tag{6.6}$$

The LEQ and the WS are separated by a drift section. However, since K-modulation calculates the average β of an LEQ, β also needs to be transferred through one half of the corresponding LEQ. The magnetic effect of an LEQ can be approximated to be constant over the LEQ so the center of the LEQ is chosen as the point where β reaches its average value. Note that the defocusing LEQ in SS 68, on which the method was tested, will work as a focusing quadrupole in the vertical plane. Similar to the tune, the value of α from MAD-X will be taken and a Gaussian error of $\sigma_\alpha = 10^{-3}$ is applied to simulate actual machine conditions. Relation 6.6 allows for the use of the variance formula

$$\sigma_f = \sqrt{\left(\frac{\partial f}{\partial x}\right)^2 \sigma_x^2 + \left(\frac{\partial f}{\partial y}\right)^2 \sigma_y^2 + \ldots}. \tag{6.7}$$

With this, the β-function and its uncertainty can be propagated from LEQ 68 to WS 68. The results for the systematic transfer factor error is shown on Fig. 6.5. The same relative error dependency is present at LEQ 68. Since the size of the error on the transfer factor is currently unknown, the accuracy of the β-function cannot be confidently less than 1 % until the transfer function of the LEQ near the iron yoke of a MU is investigated.

Figure 6.6 and Table A.1 show the dependency of the β-function on the modulation amplitude, expressed in relative terms to its maximum value, and the number of cycles assuming that there is no transfer factor error. The black line, which represents the threshold for an accuracy of 1 %, is easily reached for cases with over 20 cycles and where over 40% of the maximum amplitude is used.

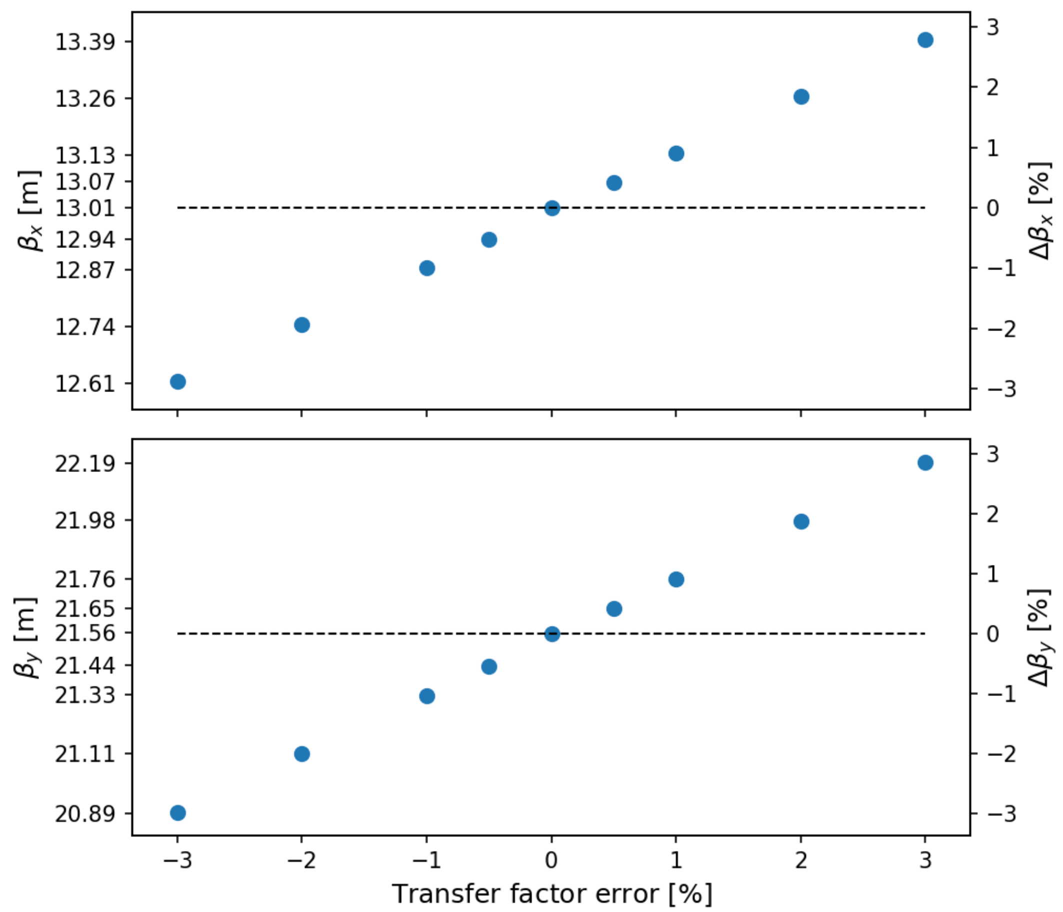

FIGURE 6.5: Impact of the uncertainty of the transfer factor on the propagated β-function at WS 68.

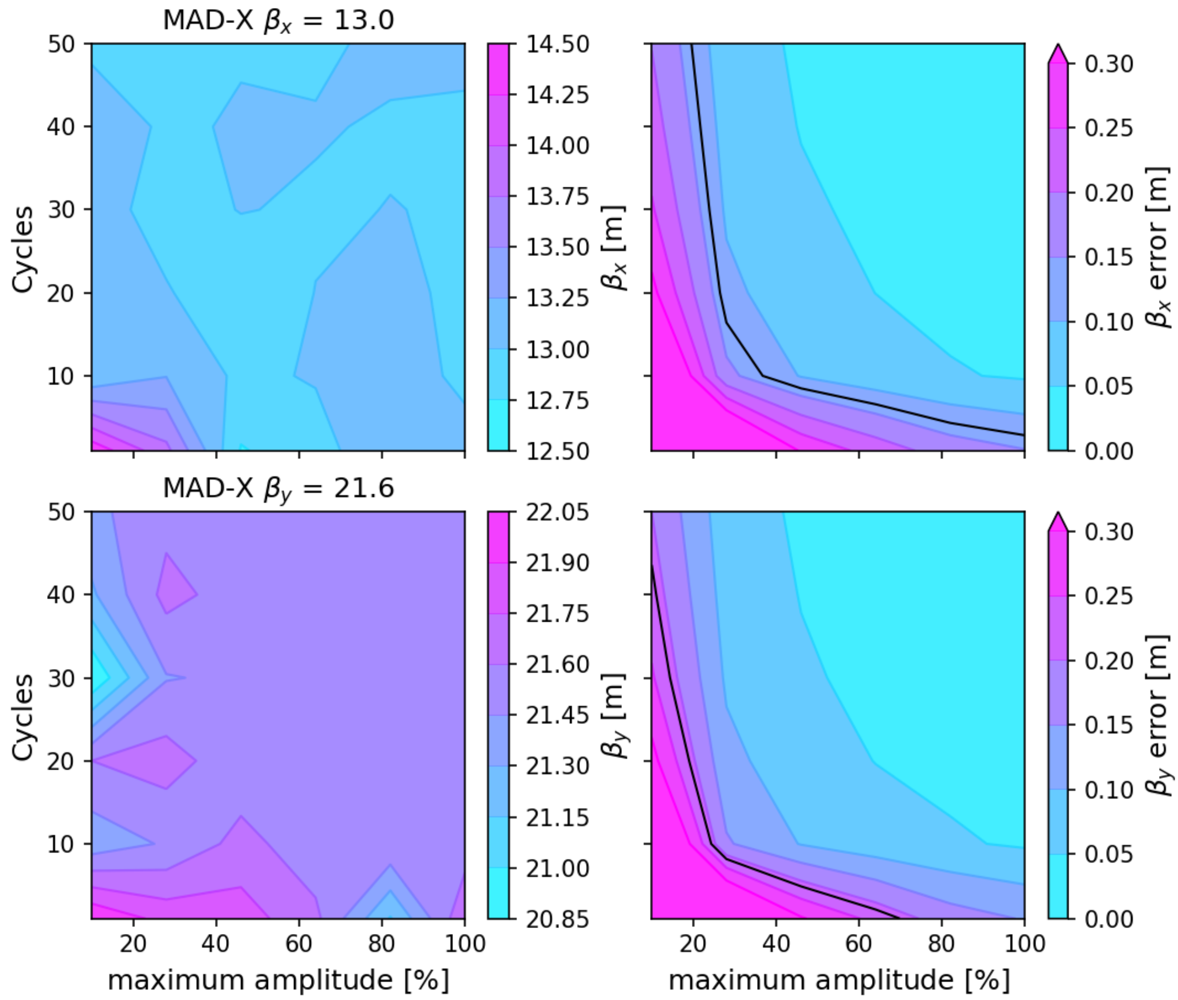

FIGURE 6.6: The dependence of the propagated β-function at WS 68 on the modulation amplitude and number of cycles. The black line represents an accuracy of 1%.

6.2 Conclusion

In the previous chapter a method was conceptualised to remove dispersive contributions from emittance measurements. In this chapter, the emphasis was on the accuracy of the measurement of the betatronic contributions, which can be improved through investigating the uncertainty of K-modulation measurements of the $\bar{\beta}$-function at an LEQ, and by propagating these values to a beam measurement location. This led to a better understanding of the typical uncertainties one can expect for a given number of cycles and the amplitude of the modulation. The impact of an error in the transfer factor of the LEQ was also investigated and it proved to be significant enough to justify additional measurements of the LEQ transfer function near the iron yoke of an MU.

7 Conclusions and Outlook

The PS experiences emittance blow-up for working points near the integer resonances, as well as during injection for LHC-type beams. The former is caused by optics beating induced by LEQs, while the latter is an accumulation of many sources. To improve the understanding of emittance blow-up at injection, the emittance measurements are required to improve in accuracy.
The research conducted in this thesis examined re-positioning of the LEQs to reduce the optics beatings, and therefore the emittance blow-up. A quantification of the optics beatings led to new possible quadrupole placings through numerical optimisation and by iteratively making one change to the current lattice. The impact of these configurations on the emittance blow-up was tested and they showed notable improvement. Especially keeping LEQ 90 at zero strength looks promising and, due to its simple testability, is going to be tested in an experimental setup once beam is again circulating in the PS after LS2. Furthermore, a zero-dispersion optics was developed as means to deconvolute the dispersive contributions from horizontal beam profile measurements around the PS, thus increasing the accuracy of the measurement. Zero-dispersion optics are achieved through minimal perturbation of the nominal optics since only the LEQs that have the biggest impact on the dispersion are used. Starting from the obtained strength configurations followed by experimentally improving the setup by looking for the minimal beam size using different knob values, zero dispersion optics should be reachable inside the machine.
Additionally, the accuracy of measurements of the β-functions used to infer the transverse emittances were studied. The $\bar{\beta}$ of an LEQ is achieved through K-modulation and propagated to a WS. Depending on the modulation amplitude and the number of cycles used to calculate β, a precision of 1 % or less can be achieved. Yet, the unknown error on the transfer factor causes a directly proportional relative error on the knowledge of the β-function at the WS. Therefore, an additional measurement of the transfer function is required.

A Supporting Tables

relative β_x precision [%]	Amplitude [%]					
cycle(s)	10	28	46	64	82	100
1	10.7	3.56	2.26	1.75	1.34	1.17
10	3.48	1.24	0.75	0.54	0.41	0.35
20	2.42	0.87	0.53	0.38	0.29	0.24
30	1.96	0.71	0.44	0.31	0.24	0.20
40	1.71	0.62	0.37	0.27	0.21	0.17
50	1.52	0.54	0.33	0.24	0.19	0.15

relative β_y precision [%]	Amplitude [%]					
cycle(s)	10	28	46	64	82	100
1	6.45	2.15	1.36	1.06	0.81	0.70
10	2.10	0.75	0.45	0.32	0.25	0.21
20	1.46	0.52	0.32	0.23	0.18	0.15
30	1.19	0.43	0.26	0.19	0.14	0.12
40	1.03	0.37	0.22	0.16	0.13	0.10
50	0.92	0.33	0.20	0.15	0.11	0.09

TABLE A.1: The uncertainty on the β-functions at WS 68 relative to the MAD-X β value, with respect to the maximum amplitude and the number of measurement cycles. The corresponding β-values are shown on Fig. 6.6

$[mT/m]$	SEM 48	SEM 52	SEM 54	WS 54	WS 65	WS 68	BGI 82
LEQ 5	-5.35	-5.35	4.75	5.07	-4.35		
LEQ 6	-3.31	-3.31					
LEQ 9					-3.93	-4.54	-5.37
LEQ 17					3.85	5.06	5.79
LEQ 18						3.15	
LEQ 21	-5.24	-5.24	4.48	4.80	-4.32		
LEQ 22	-3.29	-3.29					
LEQ 27			-5.59	-5.21		-4.60	
LEQ 28			-3.56	-3.33			
LEQ 31	4.90	4.90			5.64		5.66
LEQ 32							3.64
LEQ 35			5.09	5.09		5.09	
LEQ 36			3.07	3.26			
LEQ 39	-5.25	-5.25			-5.77		-5.21
LEQ 40							-3.29
LEQ 45	5.18	5.18	-5.56	-5.43	3.95		
LEQ 46	3.32	3.32					
LEQ 49	5.59	5.59			4.37	4.69	6.01
LEQ 50						3.04	
LEQ 55			5.17	5.25	-5.85		-5.15
LEQ 56				3.05			-3.39
LEQ 59	-4.78	-4.78				-4.69	
LEQ 67	4.75	4.75			5.89	5.09	
LEQ 71			4.97	5.06		4.22	-5.07
LEQ 72				3.02			-3.34
LEQ 77			-3.36		-3.42	-4.90	
LEQ 78			-2.98			-2.91	
LEQ 81	5.31	5.31	-4.78	-4.73	4.60		5.80
LEQ 85					3.80	5.11	5.78
LEQ 86						3.09	
LEQ 89	-5.35	-5.35	4.51	4.84	-4.48		
LEQ 90	-3.23	-3.23					
LEQ 95			-5.63	-5.26		-4.60	
LEQ 96			-3.52	-3.32			
LEQ 99	5.06	5.06			5.89		5.98
LEQ 100							3.65

TABLE A.2: The integrated normalised LEQ strengths, in mT/m, to reach zero dispersion optics with 15 active LEQs at the beam profile measurement location above. The resulting optics are shown in Fig. 5.5.

Bibliography

[1] K. Wille and J. McFall. *The Physics of Particle Accelerators: An Introduction*. The Physics of Particle Accelerators: An Introduction. Oxford University Press, 2000. ISBN: 9780198505495.

[2] Philip J. Bryant and Kjell Johnsen. *The Principles of Circular Accelerators and Storage Rings*. Cambridge University Press, 1993. DOI: 10.1017/CBO9780511563959.

[3] A. Latina. "Introduction to Transverse Beam Dynamics". In: (JUAS - 2020). Archamps, France, 2020.

[4] R. Williamson. "Lecture 7: Momentum Effects". In: (Michaelmas Term 2019). online, 2019.

[5] H. Bartosik. "Linear imperfections and correction". In: (JUAS - 2020). Archamps, France, 2020.

[6] A. Huschauer. "Working point and resonance studies at the CERN Proton Synchrotron". Presented 10 Oct 2012. 2012. URL: https://cds.cern.ch/record/1501943.

[7] A. Huschauer. "Beam Dynamics Studies for High-Intensity Beams in the CERN Proton Synchrotron". Presented 17 Jun 2016. 2016. URL: https://cds.cern.ch/record/2194332.

[8] H. Braun. "Emittance Diagnostics I, II". In: (CAS - 2008). Dourdan, France, 2008.

[9] M. Ferrario, M. Migliorati, and L. Palumbo. "Space Charge Effects". In: arXiv:1601.05214. arXiv:1601.05214 (2016). 26 pages, contribution to the CAS - CERN Accelerator School: Advanced Accelerator Physics Course, Trondheim, Norway, 18-29 Aug 2013, 331–356. 26 p. DOI: 10.5170/CERN-2014-009.331. URL: https://cds.cern.ch/record/1982426.

[10] M. Migliorati. "Space Charge Effects and Instabilities". In: (JUAS - 2020). Archamps, France, 2020.

[11] *MAD Web Page*. 2020. URL: http://madx.web.cern.ch/madx/ (visited on 12/28/2020).

[12] L. Deniau H. Grote F. Schmidt and G. Roy. *User's Reference Manual*. 2020. URL: https://mad.web.cern.ch/mad/webguide/manual.html.

[13] W. Herr and F. Schmidt. *A MAD-X Primer*. 2004. URL: https://cds.cern.ch/record/744163.

[14] *CERN Optics Repository*. 2020. URL: https://acc-models.web.cern.ch/acc-models/ (visited on 12/29/2020).

[15] H. Bartosik A. Huschauer M. Kaitatzi H. Rafique F. Asvesta. "MD4224 High Brightness". In: (Space charge meeting: PS integer experiment). CERN, 2019.

[16] H. Bartosik A. Huschauer M. Kaitatzi H. Rafique F. Asvesta. "Approaching the Integer Tune in the Proton Synchrotron to Probe Space Charge at Injection". In: (LIU-PS Beam Dynamics WG meeting 36). CERN, 2019.

[17] H. Rafique. *MD4224 Light github repository*. forked on 26-07-2020. URL: https://github.com/HaroonRafique/MD4224_Light.

[18] A. Shishlo et al. "The Particle Accelerator Simulation Code PyORBIT". In: *Procedia Computer Science* 51 (2015). International Conference On Computational Science, ICCS 2015, pp. 1272 –1281. ISSN: 1877-0509. DOI: https://doi.org/10.1016/j.procs.2015.05.312.

[19] E. Regenstreif. *The CERN Proton Synchrotron Part 2*. CERN Yellow Reports: Monographs. French version published as CERN 59-26. Geneva: CERN, 1960. DOI: 10.5170/CERN-1960-026. URL: https://cds.cern.ch/record/102347.

[20] E. Regenstreif. *The CERN Proton Synchrotron Part 1*. CERN Yellow Reports: Monographs. French version published as CERN 58-06. Geneva: CERN, 1959. DOI: 10.5170/CERN-1959-029. URL: https://cds.cern.ch/record/214352.

[21] Jean-Paul Burnet et al. *Fifty years of the CERN Proton Synchrotron: Volume 1*. CERN Yellow Reports: Monographs. Geneva: CERN, 2011. DOI: 10.5170/CERN-2011-004. URL: https://cds.cern.ch/record/1359959.

[22] *Normal straight length 401 with covers assy*. Tech. rep. URL: https://edms.cern.ch/document/2259670/AA.

[23] P. Bossard. *Etude et realisation de quadrupoles d'injection*. Tech. rep. URL: https://edms.cern.ch/document/1751471/1.

[24] P Bossard. *Technical specification: Specification for standard quadrupole magnets for the injection lines to the CERN 28 GeV proton synchrotron and the booster injector*. Tech. rep. CERN-SI-Int-MAE-69-7. Geneva: CERN, 1969. URL: https://cds.cern.ch/record/1329472.

[25] P Freyermuth et al. "CERN Proton Synchrotronworking point Matrix for extended pole face winding powering scheme". In: CERN-ATS-2010-180 (2010), 4 p. URL: https://cds.cern.ch/record/1287599.

[26] H Damerau et al. *LHC Injectors Upgrade, Technical Design Report*. Tech. rep. CERN-ACC-2014-0337. 2014. URL: https://cds.cern.ch/record/1976692.

[27] J. M. Gomes de Faria R. Chritin. *Mesures magnétiques des quadripôles d'injection qNN 401, qLN 402 et quadripôles "skew" qNS 403 et qLS 404*. Tech. rep. URL: https://edms.cern.ch/document/371500/1.

[28] P. Forck. "Lecture Notes on Beam Instrumentation and Diagnostics". In: (JUAS - 2018). 2018.

[29] M Martini and Horst Otto Schönauer. "Emittance measurements in the CERN PS complex". In: *Part. Accel.* 58.CERN-PS-97-018-CA (1997), 137–151. 16 p. URL: https://cds.cern.ch/record/324553.

[30] V Agoritsas et al. *The fast wire scanner of the CERN PS*. Tech. rep. CERN-PS-95-06-BD-OP. Geneva: CERN, 1995. URL: https://cds.cern.ch/record/319333.

[31] J.L. Sirvent et al. "Performance Assessment of Pre-Series Fast Beam Wire Scanner Prototypes for the Upgrade of the CERN LHC Injector Complex". In: *Proc. of International Beam Instrumentation Conference (IBIC'17)* (Grand Rapids, MI, USA). 6. Geneva, Switzerland: JACoW, 2018, pp. 338–341. ISBN: 978-3-95450-192-2. DOI: https://doi.org/10.18429/JACoW-IBIC2017-WEPCC03.

[32] P Elmfors et al. "Wire scanners in low energy accelerators". In: *Nuclear Instruments and Methods in Physics Research Section A: Accelerators, Spectrometers, Detectors and Associated Equipment* 396.1-2 (1997), 13–22. ISSN: 0168-9002. DOI: 10.1016/s0168-9002(97)00726-2.

[33] *Proton Synchrotron Optics Repository*. 2020. URL: https://acc-models.web.cern.ch/acc-models/ps/ (visited on 12/29/2020).

[34] Jorge Nocedal and Stephen J. Wright. *Numerical Optimization*. second. New York, NY, USA: Springer, 2006.

[35] Stephen Boyd and Lieven Vandenberghe. *Convex Optimization*. Cambridge University Press, 2004. DOI: 10.1017/CBO9780511804441.

[36] Fiala J. Marteau B. Cartis C. and L. Roberts. "Improving the Flexibility and Robustness of Model-Based Derivative-Free Optimization Solvers". In: *ACM Transactions on Mathematical Software* (2019), pp. 32:1–32:41.

[37] Fernando Nogueira. *Bayesian Optimization: Open source constrained global optimization tool for Python*. 2014–. URL: https://github.com/fmfn/BayesianOptimization.

[38] Yu-Ren Liu et al. *ZOOpt: Toolbox for Derivative-Free Optimization*. 2018. arXiv: 1801.00329 [cs.LG].

[39] *Scipy.optimize*. 2008–2020. URL: https://docs.scipy.org/doc/scipy/reference/tutorial/optimize.html.

[40] H Bartosik and G Rumolo. "Beams from the injectors". In: (2017), 233–238. 6 p. URL: https://cds.cern.ch/record/2293681.

[41] V. Forte et al. "Overview of the CERN PSB-to-PS Transfer Line Optics Matching Studies in View of the LHC Injectors Upgrade Project". In: *Proc. 61st ICFA Advanced Beam Dynamics Workshop (HB'18), Daejeon, Korea, 17-22 June 2018*. Geneva, Switzerland: JACoW Publishing, pp. 272–277. ISBN: 978-3-95450-202-8. DOI: doi:10.18429/JACoW-HB2018-WEP2PO006.

[42] F. Antoniou. "Brightness and transverse emittance from the PSB". In: (Session 1 preparatory meeting for LIU Workshop). CERN, 2019.

[43] M. Fraser. "Update on turn-by-turn measurements with SEM grids". In: (LIU-PS Beam Dynamics WG meeting 31). CERN, 2019.

[44] *Beam parameters at injection of each accelerator*. Tech. rep. 2017. URL: https://edms.cern.ch/document/1296306/2.

[45] H. Rafique A. Huschauer. "Zero-dispersion optics for horizontal emittance measurements". In: (LIU-PS Beam Dynamics WG meeting 38). CERN, 2019.

[46] L. Vandenberghe M. S. Andersen J. Dahl. *CVXOPT: Python Software for Convex Optimization*. 2004–. URL: http://cvxopt.org/.

[47] M Gasior and R Jones. *The principle and first results of betatron tune measurement by direct diode detection*. Tech. rep. LHC-Project-Report-853. CERN-LHC-Project-Report-853. revised version submitted on 2005-09-16 09:23:15. Geneva: CERN, 2005. URL: http://cds.cern.ch/record/883298.